A simple immersed-boundary method for solid–fluid interaction in constant- and stratified-density flows

Barbara Bigot [a,b], Thomas Bonometti [a,b,*], Laurent Lacaze [a,b], Olivier Thual [a,b]

[a] Université de Toulouse, INPT, UPS, IMFT (Institut de Mécanique des Fluides de Toulouse), Allée Camille Soula, F-31400 Toulouse, France
[b] CNRS, IMFT, F-31400 Toulouse, France

Keywords:
Immersed-boundary method
Stratified density flows
Navier–Stokes equations
Solid–fluid interaction

A B S T R A C T

The present work reports on the simulation of two- and three-dimensional constant- and stratified-density flows involving fixed or moving objects using an immersed-boundary method. The numerical approach is based on a simple immersed-boundary method in which no explicit Lagrangian marking of the immersed boundary is used. The solid object is defined by a continuous solid volume fraction which is updated thanks to the resolution of the Newton's equations of motion for the immersed object. As shown on several test cases, this algorithm allows the flow field near the solid boundary to be correctly captured even though the numerical thickness of the transition region separating the fluid from the object is within three computational cells approximately. The full set of governing equations is then used to investigate some fundamental aspects of solid–fluid interaction, including fixed and moving objects in constant and stratified-density flows. In particular, the method is shown to accurately reproduce the steady-streaming patterns observed in the near-region of an oscillating sphere, as well as the so-called Saint Adrew's cross in the far-field when the sphere oscillates in a rotating stratified fluid. The sedimentation of a particle in a stratified ambient is investigated for particle Reynolds numbers up to $\mathcal{O}(10^3)$ and the effect of stratification and density ratio is addressed. While the present paper only consider fluid–solid interaction for a single object, the present approach can be straightforwardly extended to the case of multiple objects of arbitrary shape moving in a stratified-density flow.

1. Introduction

Solid–fluid interactions are encountered in a large number of industrial and natural applications, including chemical engineering, aeronautics, transportations, biomecanics, geophysics and oceanography, to name but a few. Modeling solid–fluid interaction is often difficult because of the complexity of the solid shape and motion in the fluid flow. Reproducing the dynamics of multiple interacting objects of arbitrary geometry with possible deformation is made even more challenging if the flow is non-uniform in composition (multiphase flows), density (compressible or stratified flows) or temperature (heat transfer, phase change).

Methods for modeling solid–fluid interaction may be divided within two main groups, depending on the way the solid–fluid interfaces are described. One group, usually referred to as "body-fitted grid methods" makes use of a structured curvilinear or unstructured grid to conform the grid to the boundary of the fluid domain (see e.g. [59,41] for grid generation techniques). In situations involving complex moving boundaries, one needs to establish a new body-conformal grid at each time-step which leads to a substantial computational cost and subsequent slowdown of the solution procedure. In addition, issues associated with regridding arise such as grid-quality and grid-interpolation errors.

The second group of methods is referred to as "fixed-grid methods". These techniques make use of a fixed grid, which eliminates the need of regridding, while the presence of the solid objects is taken into account via adequately formulated source terms added to fluid flow equations. Fixed-grid methods have emerged in recent years as a viable alternative to body-conformal grid methods. In this group, one can mention distributed Lagrange multiplier with a fictitious-domain (DLM) based methods [23,51,50,65,2], immersed-boundary method (IBM) [54,20,37,63], lattice Boltzmann method (LBM) [38], penalty method [36,56] and ghost-fluid method [21] have been developed and shown to be effective in computing fluid-particle systems and fluid-structure interaction problems.

The immersed-boundary method was first introduced by Peskin [53] for computing blood flow in the cardiovascular system. In the

* Corresponding author at: Université de Toulouse, INPT, UPS, IMFT (Institut de Mécanique des Fluides de Toulouse), Allée Camille Soula, F-31400 Toulouse, France. Tel.: +33 534322952.
E-mail address: thomas.bonometti@imft.fr (T. Bonometti).

http://dx.doi.org/10.1016/j.compfluid.2014.03.030

original method the flow field is described on a fixed Eulerian grid and the immersed boundary is represented with a set of Lagrangian points on which the no-slip boundary condition is enforced by adding appropriate boundary forces. The boundary forces which are singular Dirac functions along the surface in the continuous equations are described by discrete regularization functions that smear the forcing effect over the neighboring Eulerian cells (see e.g. Fig. 2 of [44]). The immersed-boundary method has been improved since the pioneering work of Peskin and many variants can be found in the literature ([43,1], see also the reviews of [34,44]).

While immersed-boundary method has been used in a wide range of applications (compressible flows, particulate flows, micro-scale flows, multi-phase flows, conjugate heat transfer, see e.g. Kang et al. [35] and reference therein), application to stratified flows has been rare. To our knowledge, the only recently reported work using a fixed-grid approach computing the motion of rigid objects in a stratified fluid is that of Doostmohammadi and Ardekani [19] who used a DLM approach to investigate the interaction of a pair of particles sedimenting in a stratified fluid, using the Boussinesq approximation. Here we present an immersed-boundary method aimed at describing the motion of multiple objects of arbitrary shape in a constant- or stratified-density flow. The specificity of the present method is that (i) the treatment of the solid–fluid interaction is simple and easy to implement in the sense that there is no Lagrangian marking of the immersed boundary nor interpolation needed and (ii) the fluid density can be inhomogeneous, with no restriction on the density gradient, i.e. the method is applicable to non-Boussinesq flows. Details of the numerical scheme are outlined in Section 2 and the method is applied to investigate solid–fluid interaction in constant and stratified-density flows in Section 3, in which both forced motion and freely moving rigid objects are simulated.

2. Governing equations and numerical method

2.1. Governing equations and assumptions for the fluid phase

Assuming a variable-density non-diffusive Newtonian fluid, the evolution of the flow is then described using the Navier–Stokes equations, namely

$$\frac{\partial \mathbf{V}}{\partial t} + \nabla \cdot (\mathbf{V} \otimes \mathbf{V}) = \mathbf{g} - \frac{1}{\rho}\nabla P + \frac{1}{\rho}\nabla \cdot [\mu(\nabla \mathbf{V} + \nabla \mathbf{V}^T)] + \mathbf{f}, \tag{1}$$

$$\nabla \cdot \mathbf{V} = 0. \tag{2}$$

In (1) and (2), $\mathbf{V}, P, \rho$ and μ denote the local velocity, pressure, density and viscosity of the fluid, respectively, $\mathbf{g}$ denotes gravity and $\mathbf{f}$ is a volume force term used to take into account solid–fluid interaction. The local density of the non-diffusive fluid obeys

$$\frac{\partial \rho}{\partial t} + (\mathbf{V} \cdot \nabla)\rho = 0. \tag{3}$$

The detailed development of 1, 2 in the more general case of diffusive fluids can be found in Cook and Dimotakis [15]. Here, we simply set the diffusivity to zero. 1, 2 are written in a general system of orthogonal curvilinear coordinates. However, in the present work, only Cartesian or polar systems of coordinates were used. The reader is referred to Magnaudet et al. [42] for more details about the resolution of (1) and (2) in the more general system of orthogonal curvilinear coordinates.

Eqs. (1)–(3) are enforced throughout the entire domain, including the actual fluid domain and the space occupied by the immersed boundary. In the following, the term $\mathbf{f}$ will be formulated such as to represent the action of the immersed solid boundaries upon the fluid.

Here, we consider a fluid of variable density for which non-Boussinesq effects may play a role. In the general case of diffusive non-Boussinesq fluids there are some fundamental issues with the proper governing equations to be used. As discussed in Joseph and Renardy [29] and Chen and Meiburg [13] among others, divergence effects and Korteweg stresses can potentially be important in regions of large concentration gradients and need to be taken into account in physical models. These effects do not need to be included if one assumes the fluid to be non-diffusive, as in the present work. Conversely, using a non-diffusive fluid may results in sharp local density gradients which may cause computational difficulties, especially in the case of solid objects moving in a stratified fluid [60]. Here, such issues are circumvented by the use of a numerical scheme specifically designed to handle sharp gradients for the equation of transport of density, as described in Section 2.3.

2.2. Equations of motion for the solid phase

Let us consider a non-deformable solid object of density ρ_p and volume ϑ_p, the centroid of which being located at $\mathbf{x}_p$, moving at linear and angular velocity $\mathbf{u}_p$ and ω_p, respectively. Here the index "p" refers to particle label. The local velocity in the object is then defined by $\mathbf{U} = \mathbf{u}_p + \omega_p \times \mathbf{r}, \mathbf{r}$ being the local position relative to the solid centroid. As will be detailed in the next section, the volume force $\mathbf{f}$ is chosen to ensure $\mathbf{V} = \mathbf{U}$ in ϑ_p (rigid-body motion throughout the volume of the solid object). Thus, integrating momentum and kinematic momentum laws for the fluid on ϑ_p gives [63]

$$\frac{d}{dt}\int_{\vartheta_p} \rho \mathbf{V} d\vartheta = \bar{\rho}\vartheta_p \frac{d\mathbf{u}_p}{dt} = \int_{S_p} \tau \cdot \mathbf{n} dS + \int_{\vartheta_p} \rho \mathbf{f} d\vartheta + \bar{\rho}\vartheta_p \mathbf{g}, \tag{4}$$

$$\frac{d}{dt}\int_{\vartheta_p} \rho \mathbf{r} \times \mathbf{V} d\vartheta = \bar{\rho}\, \mathbf{I}_p \frac{d\omega_p}{dt} = \int_{S_p} \mathbf{r} \times (\tau \cdot \mathbf{n}) dS + \int_{\vartheta_p} \rho \mathbf{r} \times \mathbf{f} d\vartheta, \tag{5}$$

with $\tau = -P\mathbf{I} + \mu(\nabla \mathbf{V} + \nabla \mathbf{V}^T)$ being the hydrodynamic stress tensor, $\mathbf{I}_p$ the inertia matrix, $\mathbf{n}$ the outward-pointing normal vector on the solid–fluid boundary S_p and $\bar{\rho}$ the averaged fluid density in the volume occupied by the particle, *viz*

$$\bar{\rho} = \frac{1}{\vartheta_p}\int_{\vartheta_p} \rho d\vartheta. \tag{6}$$

Note that in the case of a constant-density fluid $\bar{\rho} = \rho$. The motion of the solid object can be either externally imposed or driven by its weight and the fluid forces on its boundary. In the latter case, it is described by Newton's equations for linear and angular momentum of a rigid body, namely

$$\rho_p \vartheta_p \frac{d\mathbf{u}_p}{dt} = \int_{S_p} \tau \cdot \mathbf{n} dS + \rho_p \vartheta_p \mathbf{g}, \tag{7}$$

$$\mathbf{I}_p \frac{d\omega_p}{dt} = \int_{S_p} \mathbf{r} \times (\tau \cdot \mathbf{n}) dS. \tag{8}$$

In order to ensure that the fictitious body force $\mathbf{f}$ is such that (7) and (8) are equivalent to (4) and (5), respectively, we obtain the following equations of motion *viz*

$$\frac{d\mathbf{u}_p}{dt} = \mathbf{g} - \frac{1}{(\rho_p - \bar{\rho})\vartheta_p}\int_{\vartheta_p} \rho \mathbf{f} d\vartheta, \tag{9}$$

$$\mathbf{I}_p \frac{d\omega_p}{dt} = -\frac{\rho_p}{(\rho_p - \bar{\rho})}\int_{\vartheta_p} \rho \mathbf{r} \times \mathbf{f} d\vartheta. \tag{10}$$

2.3. Spatial discretization and time-integration of the full system of equations

Our computational procedure employs a finite-volume approach on a staggered grid [31]. The transport equation of the

density (3) is solved by using a modified version of the transport scheme proposed by Zalesak [67], which belongs to the family of Flux Corrected Transport schemes [7]. This flux-limiting scheme combines the use of a low-order and a high-order expression of the flux to guarantee the positivity and monotonicity of ρ. This so-called shock-capturing scheme allows for the computation of large density gradients present in incompressible non-miscible flows [6] or non-diffusive miscible flows as in the present work. The algorithm is not detailed here, as it is extensively described in the original reference Zalesak [67] as well as in several textbooks. Here we use first- and eight-order approximations for the low- and high-order fluxes, respectively.

The time integration of momentum equation for the fluid (1) and (2) and the solid (9) and (10) is performed via a third-order low-storage Runge–Kutta method for all terms except the viscous term for which a second-order semi-implicit Crank–Nicolson scheme is used [55]. Advective and diffusive terms are evaluated with a second-order centered scheme (see [42] for the details concerning the treatment of advective fluxes and normal stresses). The incompressibility condition (2) is satisfied through a projection method. Briefly, the projection method consists in decomposing the velocity field into two parts, one being a function of an auxiliary potential function as (21). Using this decomposition together with the divergence-free property of the velocity field, one gets a Poisson pseudo-Eq. (19) for the pressure which becomes a substitute for the incompressibility condition (2). Following and modifying the original proposal of Le and Moin [39], Calmet [9] showed that the Poisson equation does not need to be solved at each intermediate time step of the Runge–Kutta scheme. Thus it is solved only once at the end of the complete time step, without altering the temporal accuracy of the scheme. Note that there is a substantial literature which expands the present choices regarding projection methods for constant-density flows [8,25, and reference therein] and more recently for variable-density flows [26]. The Poisson linear system is solved thanks to a Preconditioned Conjugate Gradient method from the PETSc library [4], with a preconditioner using the Block–Jacobi method. Note that computational time used for the resolution of the Poisson equation in the present variable-density problem is about 80% of the total computational time. More details about the numerical procedure used in the case where there is no immersed object, i.e. $\mathbf{f} = 0$, can be found in Calmet and Magnaudet [10]. Domain decomposition and Message-Passing-Interface (MPI) parallelization is performed to facilitate simulation of large number of computational cells.

2.4. Calculation of the forcing term for the coupling of the solid–fluid interaction

Recent progress about the computation of solid–fluid interaction have been made within the last decade (see e.g. [34,44] for comprehensive reviews), leading to several approaches which differ from the way the forcing term $\mathbf{f}$ is evaluated. The direct and indirect forcing methods have emerged as the most popular variants in this regard. Besides eliminating the time step restriction, direct forcing does not require any empirical constants.

In general, the shape of the solid object is complex and the location of the boundary condition for the velocity is unlikely to coincide with the grid nodes, so that interpolation techniques are usually employed to enforce the boundary condition by imposing constraints on the neighboring grid nodes. Here we adopt another strategy. We introduce a function α denoted as "solid volume fraction", which is equal to one in cells filled with the solid phase, zero in cells filled with the fluid phase, and $0 < \alpha < 1$ in the region of the boundary. In practice, the transition region is set-up to be of one-to-three grid cells approximately [66]. The typical expression of the forcing term reads

$$\mathbf{f} = \alpha \frac{\mathbf{U} - \widetilde{\mathbf{V}}}{\Delta t}, \tag{11}$$

where Δt is the time step used for the time-advancement, $\mathbf{U}$ is the local velocity imposed to the immersed solid object, and $\widetilde{\mathbf{V}}$ is a predictor velocity without considering the immersed object, the calculation of which depends on the numerical scheme used to solve (1). The specific definition of $\mathbf{f}$ and $\widetilde{\mathbf{V}}$ used in the time-marching scheme of the present work is given in the next section.

Using the solid volume fraction α in (11), which may be viewed as a smoothing of the immersed boundary, is an alternative way to using a regularizing function in conjunction with a Lagrangian marking of the boundary. The latter technique is largely used in immersed-boundary methods in order to allow for a smooth transfer of momentum from the boundary to the fluid (see e.g. [20,63]). The advantage of the present choice is that (i) it is simple to implement, (ii) no interpolation is needed between the Eulerian grid and possible Lagrangian markers, since no marker are used here, so that the computational cost is reduced when multiple objects are simulated, and (iii) the results are in good agreement with respect to other available higher-order immersed-boundary or boundary-fitted approaches, as will be shown later.

2.5. Summary of the time-advancement procedure

The detailed time-advancement procedure of the coupled system within a time-step is described in the following.

1. At the beginning of the time step, the divergence-free velocity field $\mathbf{V}^n$, density ρ^n, pressure $P^{n-1/2}$ in the fluid are known, as well as the position $\mathbf{x}_p^n$, linear velocity $\mathbf{u}_p^n$ and angular velocity ω_p^n of the solid.
2. ρ^{n+1} is computed by solving (3), and second-order approximations of the density field $\rho^{n+1/2}$ at time $(n+1/2)\Delta t$ are computed using $\rho^{n+1/2} = (\rho^n + \rho^{n+1})/2$, and used to solve the momentum equation. For clarity $\rho^{n+1/2}$ will be referred to as ρ.
3. Mixed Runge–Kutta/Crank–Nicolson loop ($k = 1, 2, 3$)

3a. Computation of an intermediate velocity field $\widetilde{\mathbf{V}}^k$ without considering fluid–solid interaction:

$$\frac{\widetilde{\mathbf{V}}^k - \widehat{\mathbf{V}}^{k-1}}{\Delta t} = \mathcal{SM}, \tag{12}$$

with

$$\mathcal{SM} = \gamma_k \mathbf{N}(\widehat{\mathbf{V}}^{k-1}) + \zeta_k \mathbf{N}(\widehat{\mathbf{V}}^{k-2}) + (\alpha_k + \beta_k)\mathbf{L}(\widehat{\mathbf{V}}^{k-1}) - (\alpha_k + \beta_k)\left(\frac{1}{\rho}\nabla P^{n-1/2} - \mathbf{g}\right), \tag{13}$$

where $\mathbf{N}$ (resp. $\mathbf{L}$) is a non-linear (resp. linear) operator containing the advective and viscous terms, α_k, β_k, γ_k and ζ_k are the Runge–Kutta coefficients.

3b. Modification of the velocity field in order to include the contribution of the fluid–solid coupling term $\mathbf{f}^k$ (the calculation of which does not make use of an internal loop) as,

$$\mathbf{f}^k = \alpha \frac{\mathbf{U}^{k-1} - \widetilde{\mathbf{V}}^k}{\Delta t}, \tag{14}$$

$$\frac{\widehat{\mathbf{V}}^k - \widehat{\mathbf{V}}^{k-1}}{\Delta t} - \beta_k \mathbf{L}(\widehat{\mathbf{V}}^k - \widehat{\mathbf{V}}^{k-1}) = \mathcal{SM} + \mathbf{f}^k. \tag{15}$$

3c. When not externally imposed, calculation of the linear and angular momentum of the solid object

$$\frac{\mathbf{u}_p^k - \mathbf{u}_p^{k-1}}{\Delta t} = (\alpha_k + \beta_k)\mathbf{g} - \frac{\rho}{(\rho_p - \rho)\vartheta_p}\int_{\vartheta_p} \mathbf{f}^k d\vartheta, \tag{16}$$

$$\mathbf{I}_p \frac{\omega_p^k - \omega_p^{k-1}}{\Delta t} = -\frac{\rho\rho_p}{(\rho_p - \rho)}\int_{\vartheta_p} \mathbf{r} \times \mathbf{f}^k d\vartheta. \tag{17}$$

3d. When not externally imposed, calculation of the solid position (and solid volume fraction) via,

$$\frac{\mathbf{x}_p^k - \mathbf{x}_p^{k-1}}{\Delta t} = (\alpha_k + \beta_k)(\mathbf{u}_p^k + \mathbf{u}_p^{k-1})/2. \tag{18}$$

3e. Computation of $\mathbf{U}^k = \mathbf{u}_p^k + \omega_p^k \times \mathbf{r}$.

4. For $k = 3, \widehat{\mathbf{V}}^{n+1}, \mathbf{x}_p^{n+1}, \mathbf{u}_p^{n+1}$ and ω_p^{n+1} are then obtained. A Poisson pseudo-equation is then solved to get the potential auxiliary function Φ^{n+1} as,

$$\nabla \cdot \left(\frac{1}{\rho}\nabla\Phi^{n+1}\right) = \frac{1}{\Delta t}\nabla \cdot \widehat{\mathbf{V}}^{n+1}. \tag{19}$$

5. The pressure $P^{n+1/2}$ and the divergence-free velocity $\mathbf{V}^{n+1}$ are then obtained from the potential auxiliary function Φ^{n+1}

$$P^{n+1/2} = P^{n-1/2} + \Phi^{n+1}, \tag{20}$$

$$\mathbf{V}^{n+1} = \widehat{\mathbf{V}}^{n+1} - \frac{\Delta t}{\rho}\nabla\Phi^{n+1}. \tag{21}$$

6. Return to step 1.

3. Results

In the following section, examples of fluid–solid interaction are presented in various configurations from static objects in a constant density flow toward objects moving in a stratified flow. We will focus in the present work on the dynamics of a single spherical object in a fluid. The general case of multiple interacting objects of more complex shapes will not be detailed here and is left to future work.

Let a sphere (or equivalently a cylinder in two dimensions) of radius R (diameter D), position $\mathbf{x}_p$, translational velocity $\mathbf{u}_p$ and angular velocity ω_p, surrounded by a fluid of density ρ and dynamic viscosity μ. We define the solid volume fraction α following Yuki et al. [66] *viz*

$$\alpha(\mathbf{x}) = \frac{1}{2}\left\{1 - \tanh\left(\frac{\|\mathbf{x} - \mathbf{x}_p\| - R}{\lambda\eta\Delta}\right)\right\}, \tag{22}$$

$$\lambda = |n_x| + |n_y| + |n_z|, \tag{23}$$

$$\eta = 0.065(1 - \lambda^2) + 0.39, \tag{24}$$

where $\mathbf{n} = (n_x, n_y, n_z)$ is a normal outward unit vector at a surface element, η is a parameter controlling the 'thickness' of the transition region and Δ is a characteristic grid size ($\Delta = \sqrt{2}\Delta x$ when the grid is uniform). Note that the coefficients used in (24) are 1.3 time larger than those reported in Yuki et al. [66]. Numerical tests of moving cylinders at moderate Reynolds number showed that the present set of coefficient is sufficient to suppress parasitic fluctuations of the forces applied to the objects when the latter cross a numerical cell (not shown here). A detailed discussion of this point can be found in Uhlmann [63]. Iso-contours of α as defined in (22) are shown in Fig. 8a. With the present choices, the transition region is of three grid cells approximately.

3.1. Constant-density flows

3.1.1. Flow around a cylinder at moderate Reynolds number

In the present section, we consider a fixed cylinder in a uniform flow for various Reynolds numbers in the range $1 \leqslant Re \leqslant 50$. Here, the Reynolds number is defined as,

$$Re = \rho U_0 D/\mu, \tag{25}$$

U_0 being the far-upstream velocity. For this range of Reynolds number, the wake is symmetrical along the mid-plane parallel to the flow direction x so that only half of the domain can be used. A computational (x, y)-domain of $30D \times 12D$ size with a regular grid is used, with free-slip boundary conditions on the top and bottom walls, inflow and outflow conditions along the left and right boundaries, respectively. The simulations were run from an initial uniform velocity field until steady state was reached. Several grid resolutions were used in order to investigate the sensitivity of the solution to the spatial resolution, namely $D/\Delta x = D/\Delta y = 5$, 10, 20 and 40.

The cylinder drag coefficient obtained with the present method is plotted in Fig. 1 as a function of the Reynolds number. Here, the drag coefficient is computed as,

$$C_D = \frac{F_D}{\frac{1}{2}\rho U_0^2 D}, \tag{26}$$

$$F_D = \sum_{k=1}^{3}\int_{\mathcal{S}_p} \rho \mathbf{f}^k \cdot \mathbf{e}_x d\mathcal{S}, \tag{27}$$

$\mathbf{f}^k$ being defined in (14) and $\mathcal{S}_p$ the circular section of the cylinder. Very good agreement is found with respect to results obtained from experiments [62,47] or other numerical approaches [49]. The effect of the grid resolution is illustrated in Table 1 for $Re = 40$. Keeping in mind that the present method does not use any high-order interpolation technique or marking of the boundary, a monotonous order-one-convergence is observed toward the reference value of Park et al. [49] (see the inset in Fig. 1). The steady-state vorticity contours and streamlines from the case $D/\Delta x = 40$ are shown in Fig. 2. For comparison the results of Taira and Colonius's [58] immersed-boundary method which makes use of Lagrangian markers to impose the no-slip condition at the cylinder surface, are reproduced here. The flow profiles are in close agreement with those reported by these authors. In particular, the wake properties are compared in Table 2 against previous experimental and numerical studies. Reasonable agreement is also found.

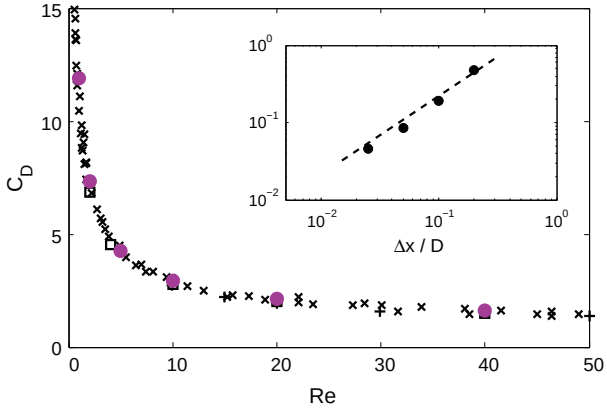

Fig. 1. Drag coefficient for a cylinder in a uniform flow for $1 \leqslant Re \leqslant 50$. Experiments: ×, [62]; +, Nishioka and Sato [47]. Numerical simulations: □, Park et al. [49]; ○, present method (two-dimensional simulations). Present results are shown for a grid resolution of $D/\Delta x = 20$. Inset: Error as a function of spatial resolution for $Re = 40$. See Table 1 for details. Dashed line indicates first order convergence.

Table 1
Effect of the grid resolution on the drag coefficient ($Re = 40$). Here, we take as reference the results of Park et al. [49] in which a body-fitted C-type grid with 128 grid points along the cylinder surface were used.

$D/\Delta x$	5	10	20	40	Park et al. [49]
C_D	2.23	1.80	1.64	1.58	1.51
$\epsilon = \frac{C_D - C_{Dref}}{C_{Dref}}$	47.7%	19.2%	8.6%	4.6%	0

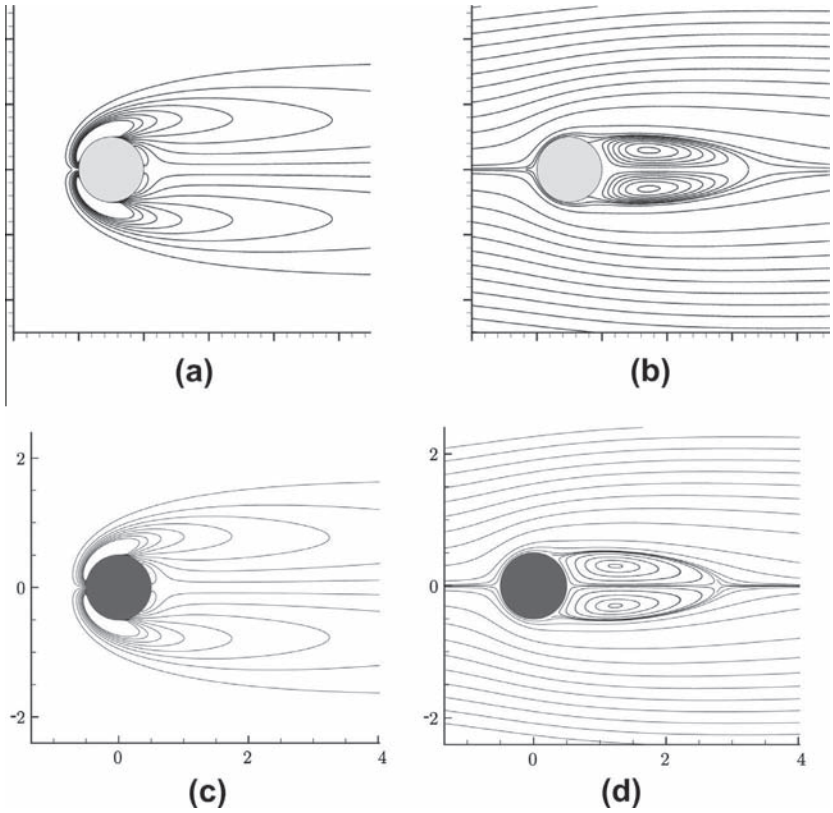

Fig. 2. Dimensionless vorticity contours (left) for steady-state flow over a cylinder at $Re = 40$, where contour levels are set from -3 to 3 in increments of 0.4, and corresponding streamlines (right). The top and bottom plots are results with the present method ($D/\Delta x = 40$, two-dimensional simulation) and those of Taira and Colonius [58], respectively. Vorticity is scaled by U_0/D, and the axis dimensions by D. Note that the streamlines are not at scale between frames (b) and (d).

Table 2
Comparison of experimental and numerical studies of steady-state wake dimensions and drag coefficient for a flow around a cylinder at $Re = 40$. l is the length of the recirculation zone measured from the rear of the sphere, a is the streamwise distance between the wake vortex core and the rear of the sphere, b is the gap between the centers of the wake vortices and θ is the separation angle measured from the rear of the sphere.

	l/D	a/D	b/D	θ (°)	C_D
Experiments					
Coutanceau and Bouard [16]	2.13	0.73	0.59	53.8	–
Tritton [62]	–	–	–	–	1.59
Numerical study					
Dennis and Chang [18]	2.35	–	–	53.8	1.52
Park et al. [49]	–	–	–	–	1.51
Linnick and Fasel [40]	2.28	0.72	0.60	53.6	1.54
Taira and Colonius [58]	2.30	0.73	0.60	53.7	1.54
Ardekani et al. [2]	2.23	–	–	–	1.55
Present method ($D/\Delta x = 40$)	2.26	0.71	0.59	54.2	1.58

3.1.2. Flow around an airfoil at $Re = 2000$

We assess in the present section the capability of the present method to capture the flow field around a non-spherical object in a regime where the flow is nearly turbulent. Results are compared with those of Hoarau et al. [33] who use a pressure-velocity based approach employing predictor-corrector pressure scheme on a conformal orthogonal curvilinear grid. The airfoil is represented by a cylinder of NACA0012 shape of length ℓ. An angle of incidence of 20° is applied to the static airfoil which is immersed in a constant-density fluid with a far-upstream velocity field $U_0\mathbf{z}, z$ being the direction of the flow in the present case. Here, the Reynolds number defined by $U_0\ell/\nu$ is set to 2000.

Part of the numerical setup is displayed in Fig. 3. The simulation is performed in a two-dimensional domain of height 10.4ℓ and length 10.4ℓ and discretized with 1200×390 grid points. The spatial resolution is uniform ($\ell/\Delta z = \ell/\Delta x = 125$) in the region $0 \leqslant z/\ell \leqslant 9.4$ and $1 \leqslant x/\ell \leqslant 4.6$ while the step size is varied following a geometric progression up to the outer walls elsewhere. Free-slip conditions are imposed at the top and bottom walls, whereas inflow and outflow conditions are set at the upstream and downstream boundaries, respectively. The tip of the airfoil is located at a distance of 2ℓ from the upstream boundary approximately.

Iso-contours of the instantaneous pressure field in the vicinity of the airfoil is displayed in Fig. 4 at time $tU_0/\ell = 14.64$ for the present immersed-boundary method and the approach of Hoarau et al. [33] using a conformal grid. In both cases, low pressure patterns are visible at the nose of the airfoil as well as in the extrados region (see the circular pattern at a distance of $\ell/3$ approximately from the extrados). The complex pressure distribution, due to the boundary-layer separation (see e.g. Fig. 3), is similar between the two methods.

Time-averaged pressure coefficient C_p distribution is plotted in Fig. 5 for three different time ranges. Here, C_p is computed as $C_p = (p - p_\infty)/0.5\rho U_0^2$, where p_∞ is the free stream pressure and p is the local pressure at the location of the immersed boundary. In the present case, we define the location of the immersed boundary as the location for which $\alpha = 0.5$. Note that we verified that the results were independent of the specific choice of α within its transition region. In all cases, a pronounced pressure plateau is observed on the upper surface of the airfoil, illustrating the presence of a separation bubble (see also Fig. 3). Depending on the time range used for averaging the the pressure coefficient, the length of the plateau somewhat varies and the pressure distribution is significantly different in the vicinity of the trailing edge, exhibiting alternatively a sharp increase (crosses) or a slight decrease (plus). In the former case, this can be attributed to the generation of a

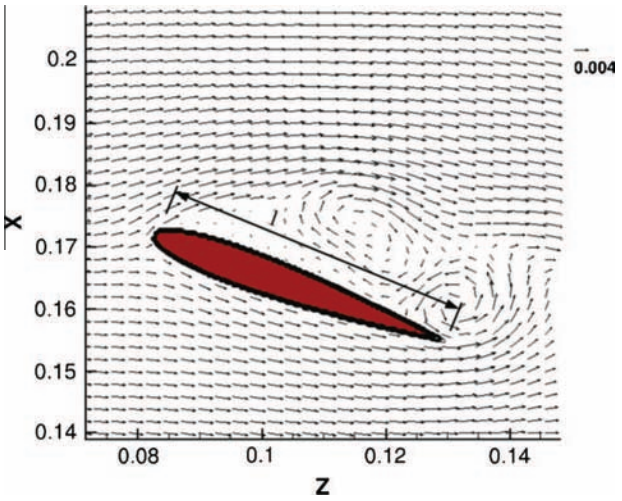

Fig. 3. Close-up view of the velocity field around the NACA0012 airfoil at time $tU_0/\ell = 14.64$. The airfoil, materialized by the iso-value of solid volume fraction $\alpha \geqslant 0.1$ is immersed in a constant-density fluid of far-upstream velocity $U_0\mathbf{z}$. Here, the simulation is two-dimensional.

strong counter-clockwise vortex at the tip of the airfoil, as the one displayed in Fig. 3, which locally increases the suction, while in the latter case the observed diminution of suction can be attributed to the expulsion of the large clockwise vortex forming the separation bubble, transported downstream the airfoil (not shown here). As expected, the pressure distribution along the intrados region is less sensitive to time-averaging. A peak is observed at the leading edge, the pressure coefficient being of order one, followed by a monotonous decrease of the pressure as one goes from the leading edge toward the trailing edge. This is in qualitative agreement with the results of Jones et al. [28] who computed the flow around a NACA0012 airfoil in a somewhat different configuration, namely $Re = 5 \times 10^4$ and an angle of incidence of 5°.

3.1.3. Oscillating sphere in a fluid initially at rest

We here consider a sphere undergoing low-amplitude oscillations at moderate Reynolds number in a constant-density flow initially at rest. This problem has been considered by Chang and Maxey [11] who highlighted the role of the Basset history force in the generation of steady streaming patterns. These authors used a pseudo-spectral method and obtained a good agreement for the time-dependent evolution of the drag coefficient compared to experiments of Odar and Hamilton [48] and the solution obtained from a force balance between the viscous Stokes drag, the inviscid added-mass force, and the Basset history force.

An oscillating motion defined by a pulsation σ and amplitude A_0 is imposed to a sphere of radius R (diameter D) in a fluid initially at rest. The sphere motion is externally given by the translational velocity

$$\mathbf{u}_p(t) = U_0 \sin(\sigma t)\mathbf{e}_z, \tag{28}$$

with $U_0 = A_0\sigma$. Note that here the motion of the object is imposed so (16)–(18) need not to be solved. The flow is controlled by two dimensionless parameters, namely the Reynolds number (as defined in (25)), and the Strouhal number $St = \sigma R/U_0$. Here we set $Re = 16.7$ and $St = 0.625$, which correspond to oscillations of amplitude $A_0 = 0.8D$.

The physical domain is a cylinder of height $20D$ and radius $10D$. Due to the axisymmetry of the flow, it is discretized with a regular two-dimensional 200×400 grid in the (r, z)-directions $(D/\Delta r = D/\Delta z = 20)$. Free-slip boundary conditions are imposed on all the walls and on the symmetry axis. Simulation is performed until the quasi-steady state is reached.

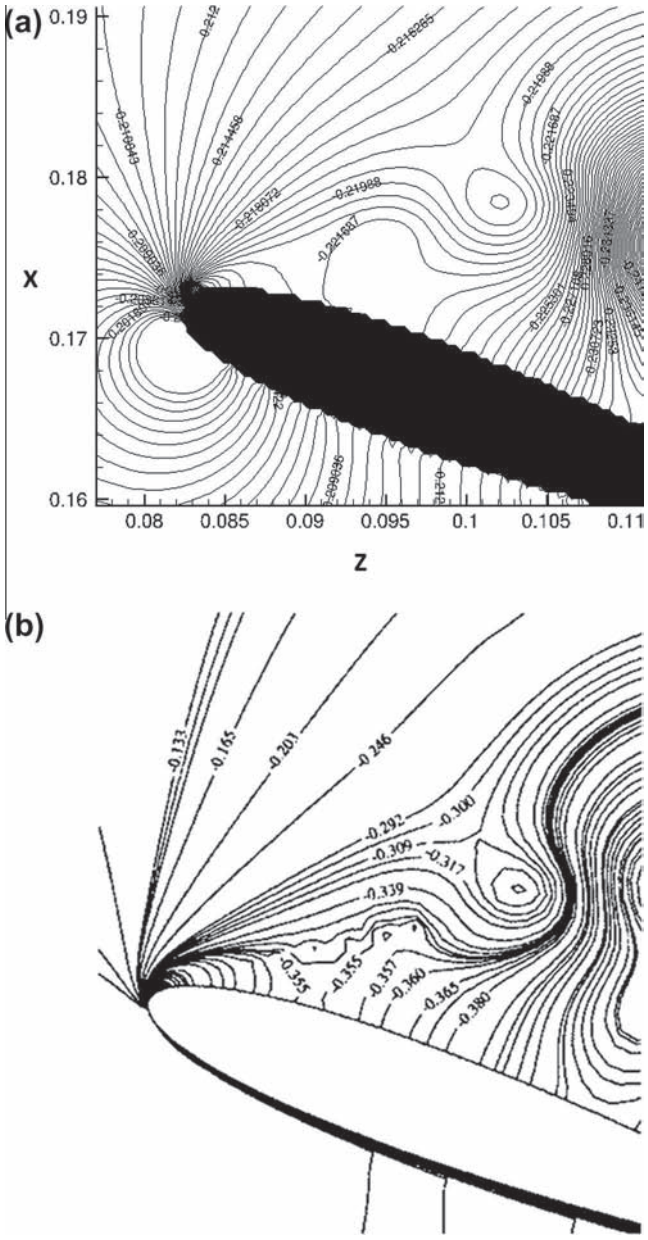

Fig. 4. Iso-contours of the instantaneous pressure field in the vicinity of the NACA0012 airfoil with an incidence angle of 20° and $Re = 2000$ for (a) the present method at $tU_0/\ell = 14.64$ and (b) results of Hoarau et al. [33].

Fig. 6 shows a sequence of vorticity contours over half an oscillation cycle. The upper (resp. lower) half of each frame is extracted from Chang and Maxey's results (resp. present results). The sequence begins just after the free-stream has reversed direction and has started to flow from right to left. Good agreement is observed throughout the whole half-cycle. The temporal evolution of the drag coefficient is plotted in Fig. 7(a) over an oscillation cycle. Here, the drag coefficient and the drag force are computed as follow

$$C_D = \frac{F_D}{\frac{1}{2}\rho U_0^2 \pi R^2}, \tag{29}$$

$$F_D = -\sum_{k=1}^{3} \int_{\vartheta_p} \rho \mathbf{f}^k \cdot \mathbf{e}_z d\vartheta. \tag{30}$$

Again, agreement is found between our present method, the pseudo-spectral approach of Chang and Maxey [11], experiments of Odar and Hamilton [48] and the analytical solution. The relative

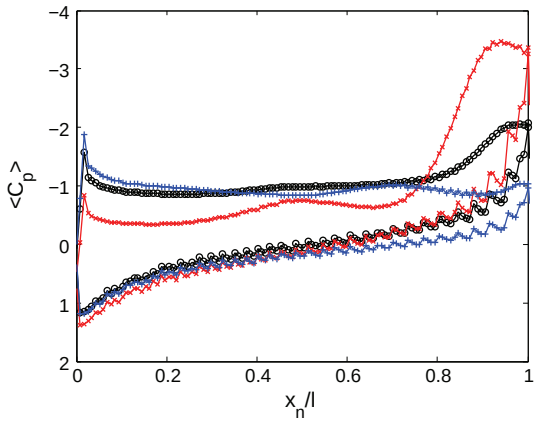

Fig. 5. Pressure coefficient C_p distribution along the airfoil extrados (upper curves) and intrados (lower curves) time-averaged in the range: $\circ, 8 \leqslant tU_0/\ell \leqslant 13.6$; $\times, 8 \leqslant tU_0/\ell \leqslant 9.2$; $+, 9.2 \leqslant tU_0/\ell \leqslant 10.4$. Here, x_n is the distance from the airfoil nose.

error computed from the maximum value of C_D at the end of the second cycle is plotted as a function of spatial resolution and time step in Fig. 7(b). A close to first- and second-order convergence is observed in time and space, respectively. Overall, this test shows that the present method is able to capture reasonably well the flow field near the immersed boundary when the latter is in motion.

3.1.4. Freely moving sphere in a viscous fluid

In this section, we assess the capability of the present approach to reproduce the free motion of an object in a constant-density viscous fluid, namely the free fall of a sphere in a liquid at rest. We set the physical properties of the object and the fluid so the density ratio is $\rho_p/\rho = 4$ and the Archimedes number $Ar = \rho(\rho_p - \rho)U_0^2 D^2/\mu^2 = 800$ with $U_0 = \sqrt{gD}$. As shown later, this corresponds to a Reynolds number, based on the terminal velocity of the sphere, of $Re = \rho u_p D/\mu = 20$ approximately.

This academic configuration allow us to compare the temporal evolution of the particle velocity with analytical solutions as well as numerical data available in the literature. Here, results are compared to those of a boundary-fitted approach which has been validated in previous papers [45,3]. This method fully resolves the flow around the falling sphere in the reference frame of the moving object, thanks to a spherical curvilinear grid which is refined in the vicinity of the rigid boundary (a close-up view of the corresponding grid is given in Fig. 8(b)). The particle motion is solved via the Kirchhoff equations of motion. In this method a $88 \times 34 \times 66$ spherical grid is used and the outer boundary are located at a distance of $20D$ from the sphere center.

Here, the simulation is performed on a two-dimensional axisymmetric (r,z)-domain of $20D \times 40D$ size with 128×800 grid points. The spatial resolution is constant along the z-direction parallel to gravity as well as in the region $0 \leqslant r/D \leqslant 1.5$ $(D/\Delta x = 20)$. For $1.5 \leqslant r/D \leqslant 20$, the grid size is varied following an arithmetic progression up to the outer wall. Free-slip boundary conditions are imposed at all boundaries. The time-step used for the simulation is $\Delta t\sqrt{g/D} = 0.04$. Fig. 8a shows the grid used and iso-contours of the solid volume fraction α defined in (22). The sphere is initially located at a distance $5R$ from the upper wall and the fluid is initially at rest.

One can estimate the initial acceleration of the sphere at early times, assuming that only the buoyancy force and the added-mass force are at play. The initial acceleration reads

$$\frac{d\mathbf{u}_p}{dt} = \frac{(\rho_p - \rho)\mathbf{g}}{\rho_p + C_M\rho}, \tag{31}$$

where C_M is the added-mass coefficient equal to 1/2 for a sphere. The sphere reaches a steady state when the drag force balances the buoyancy force. The corresponding terminal velocity of the sphere can therefore be written

$$u_p = \sqrt{\frac{|m_p - m|g}{C_D \frac{1}{2}\rho\pi R^2}}, \tag{32}$$

where m_p and m are the mass of the rigid sphere and that of the fluid contained in an equivalent volume, respectively. C_D is the drag coefficient which can be classically computed using Schiller and Naumann's correlation [14]

$$C_D = \frac{24}{Re}(1 + 0.15Re^{0.687}). \tag{33}$$

Using the definition of the Reynolds number $Re = \rho u_p D/\mu$ together with (32) and (33), one can calculate the theoretical value of the terminal velocity of the sphere.

Fig. 9 shows the temporal evolution of the sphere velocity with the boundary-fitted approach and the present immersed-boundary method. For comparison, analytical solutions (31) and (32) are also plotted. Excellent agreement is observed with respect to both the numerical and analytical solutions. The present method is shown to satisfactorily reproduce the dynamics of a free-moving object in a constant-density fluid, from the acceleration phase up to the steady-state regime.

3.2. Stratified flows

Let us consider the vertical movement of a sphere (of radius R, diameter D, characteristic velocity U_0) initially located at the vertical position z_0 in a stratified fluid. The initial stratification distribution is stable and linear such as

$$\rho(\mathbf{x}, t = 0) = \rho_0 + \frac{\partial \rho_e}{\partial z} z, \tag{34}$$

where $\frac{\partial \rho_e}{\partial z} = cte$ is the vertical gradient of the undisturbed density field, and $\rho_0 = \rho(z_0, t = 0)$ is a reference density. The corresponding hydrostatic pressure p_e reads

$$p_e(z) = -\int^z \rho g dz = -\rho_0 gz + \frac{1}{2}\frac{\partial \rho_e}{\partial z} gz(z - 2z_0). \tag{35}$$

Fluid–solid interaction depends on the Froude number $Fr = 2U_0/(ND)$ with N being the Brunt-Väisälä frequency reading

$$N^2 = -\frac{g}{\rho_0}\frac{\partial \rho_e}{\partial z}. \tag{36}$$

3.2.1. Oscillating sphere in a rotating stratified fluid

The oscillation of a sphere in a stratified fluid contained in a cylindrical tank rotating at angular velocity Ω_0 is considered here. The imposed translational and rotational velocity of the sphere in polar coordinates reads

$$\mathbf{u}_p(t) = U_0 \cos(\sigma t)\mathbf{e}_z, \tag{37}$$

$$\omega_p(t) = \Omega_0 \mathbf{e}_z, \tag{38}$$

where $U_0 = A_0\sigma$, and A_0 (resp. σ) is the amplitude (resp. pulsation) of the oscillation.

The oscillations of the sphere in the rotating stratified fluid generate both internal gravity waves due to density stratification, and inertial waves due to rotation. The structure, dynamics and interaction of these waves depend on the Froude number and the Coriolis number here defined by $\mathcal{C} = 2U_0/(\Omega_0 D)$ [24]. In particular, internal gravity and inertial waves may propagate along a specific direction, the angle ϕ of the conical wave propagation with respect

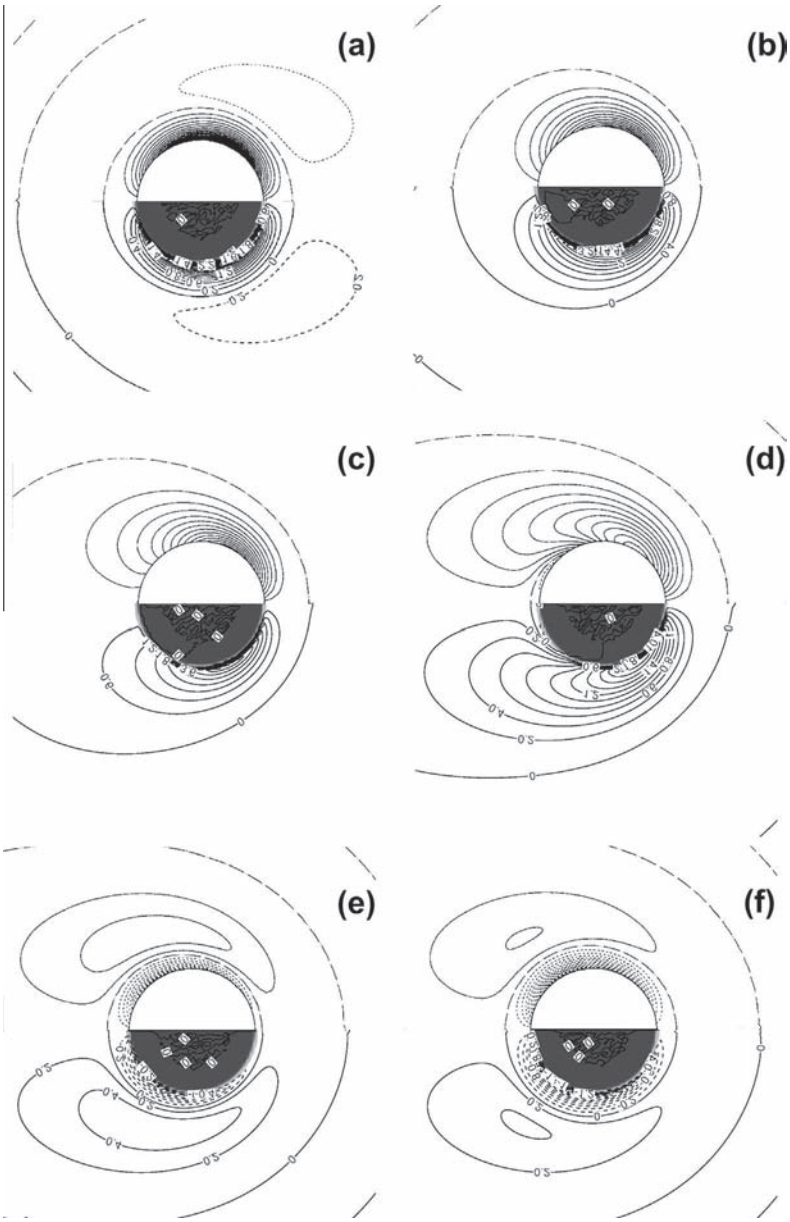

Fig. 6. Contours of the azimuthal component of vorticity ω around the sphere over half an oscillation cycle for $Re = 16.7$ and $St = 0.625$. Upper frame: Chang and Maxey's [11] simulation; Lower frame: present method (two-dimensional axisymmetric simulation). The time instance of the snapshots are such that $\sigma t = \phi[2\pi]$ with (*a*) $\phi = \pi/16, \Delta\omega = 0.2$; (*b*) $\phi = \pi/4$, $\Delta\omega = 0.4$; (*c*) $\phi = \pi/2, \Delta\omega = 0.6$; (*d*) $\phi = 3\pi/4, \Delta\omega = 0.2$; (*e*) $\phi = 15\pi/16, \Delta\omega = 0.2$; (*f*) $\phi = \pi$, $\Delta\omega = 0.2$. Dotted line: $\omega < 0$. Solid line: $\omega > 0$. Long dashed: $\omega = 0$. Here, $\Delta\omega$ is the vorticity increment between two iso-contours and ω is scaled by U_0/R.

to horizontal (r, θ)-plane obeying the following dispersion relation [32,17]

$$\sigma^2 = N^2 \sin^2 \phi + 4\Omega_0^2 \cos^2 \phi. \tag{39}$$

Note that the propagating waves only exist for excitation pulsations in the range $2\Omega_0 \leqslant \sigma \leqslant N$. In such a case, the global structure of waves resembles a cross, often referred to as Saint-Andrew cross, as evidenced by experimental observations using a Schlieren optical technique [46,57] in the case of stratified but non-rotating flows.

A three-dimensional simulation is performed with the following set of dimensionless parameters, namely $Re = \rho_0 U_0 D/\mu = 100$, $Fr = 0.8, C = 3.16$ and $A_0/R = 1$. In this peculiar case, non-linear effects are to be expected [22,64]. The present set of parameters leads to a theoretical direction of propagation of the waves obtained from (39) of $\phi \approx \pi/4$. The numerical setup is displayed in Fig. 10. The simulation is performed in a cylindrical computational domain of height $30D$, outer radius $15D$ and is discretized with $256 \times 34 \times 512$ grid points in the r, θ and z-directions, respectively. The spatial resolution is uniform along the r- and z-directions ($D/\Delta r = D/\Delta z = 20$) in the region $0 \leqslant r/D \leqslant 12.5$ and $2.5 \leqslant z/D \leqslant 27.5$ while elsewhere the grid size is varied following a geometric progression up to the outer walls. No-slip (resp. zero normal gradient) boundary conditions are imposed at all the rotating walls for the velocity (resp. density). Note that here and for all the cases with stratified fluids, no specific boundary condition is imposed to the density field at the particle surface, since the transport of the density computed via (3) is performed in the whole computational domain, including the region occupied by and surrounding the particle. The specific value of the local fluid density 'inside' the region of the particle does not play a role since here the fluid is non-diffusive. At time $t = 0$, the sphere is located in the middle of

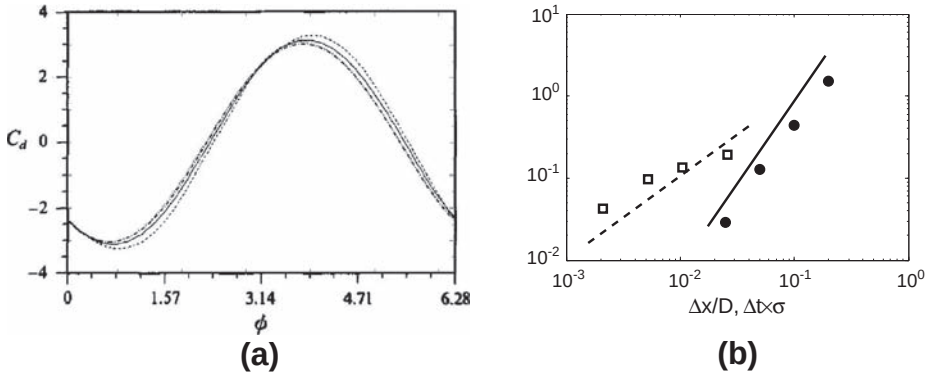

Fig. 7. (a) Time evolution of the drag coefficient C_D over an oscillation cycle: (- · - · -), present method; (_____), pseudo-spectral method of Chang and Maxey [11]; (- - - -), experiments of Odar and Hamilton [48]; (· · · · · ·), analytical solution. Here $\sigma t = \phi[2\pi]$. (b) Error computed from the maximum value of C_D at the end of the second cycle as a function of (•) spatial resolution and (□) time step. The reference value of C_D used for the spatial and temporal convergence analysis is the one obtained with $(\Delta x/D = 1.25 \times 10^{-2};\ \sigma\Delta t = 10^{-2})$ and $(\Delta x/D = 5 \times 10^{-2};\ \sigma\Delta t = 10^{-3})$, respectively. The dashed and solid lines indicate first- and second-order convergence, respectively.

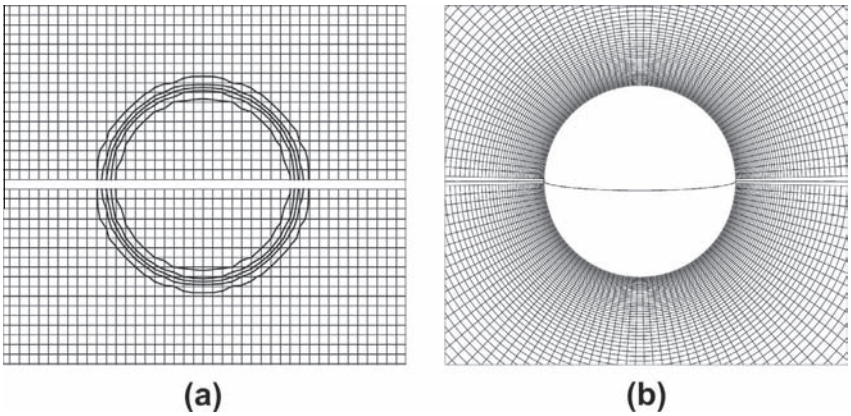

Fig. 8. Close-up view of the grid used for the simulation of the freely-falling sphere with (a) the present method and (b) a body-fitted approach. In the former (resp. latter) case, the size of the axisymmetric (resp. three-dimensional) grid is $128 \times (1) \times 800$ (resp. $88 \times 34 \times 66$) in the r, θ, z(resp. ϕ)-directions, gravity being along z-direction. In (a), the immersed boundary is materialized by iso-values of the solid volume fraction $\alpha = 0.01, 0.25, 0.5, 0.75$, and 0.99.

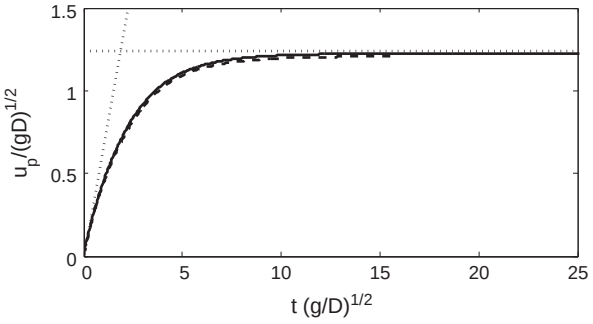

Fig. 9. Time evolution of the particle velocity: _____, present method (two-dimensional axisymmetric simulation); - - - -, boundary-fitted method, · · · · · ·, analytical solutions (31) and (32).

the computational domain at $z = z_0$, and the whole system fluid-sphere is in solid-body rotation at angular velocity Ω_0. The sphere is then set into vertical oscillatory motion according to (37).

Iso-surfaces of density fluctuations $\delta\rho$ are displayed in Fig. 11 at times $t(\sigma/2\pi) = 4.7$ and 5.2. Note that the vertical location of the sphere at these time instances is symmetrical with respect to z_0. Here $\delta\rho$ is defined as

$$\delta\rho = \frac{\rho(\mathbf{x}, t) - \rho(\mathbf{x}, t = 0)}{\rho_0}. \tag{40}$$

The iso-surfaces of density fluctuations are observed to be cones whose axis of revolution is parallel to the rotational axis/density gradient. The density fluctuations distribution mostly remains axi-symmetric and exhibits a central symmetry with respect to the averaged location of the sphere. The conical waves stemming from the generation of the internal gravity/inertia waves extend in the flow up to a distance of $10D$ from the sphere, approximately. In Fig. 12 the corresponding velocity fluctuation field $\delta\mathbf{u}$ is plotted in a chosen vertical mid-plane. Clearly, the flow exhibits a cross-shape structure, in agreement with experimental observations [22,52]. For comparison, the theoretical prediction (39) for the direction of propagation of the waves is plotted in Fig. 12 (dashed lines). Good agreement is found between the angle obtained with the present method and the analytical prediction.

The temporal evolution of the drag coefficient, here defined by $C_D = 2F_D/\rho_0\pi R^2 U_0^2$, is plotted in Fig. 13. A quasi steady-state regime is observed to rapidly take place after two periods of oscillations, the extremal values of C_D being close to ± 4. To our knowledge no numerical or experimental results on the flow characteristics such as the drag exerted on the moving sphere can be found in the literature. However, a crude comparison can be made with results of Hanazaki et al. [30] who performed numerical simulations, thanks to a boundary-fitted approach, of the flow around a vertically moving sphere in a uniformly stratified fluid for a broad range of parameters (Re, Fr, Sc), $Sc = \nu/K$ being the Schmidt number, ν the fluid kinematic viscosity and K the mass diffusivity. In the simulations

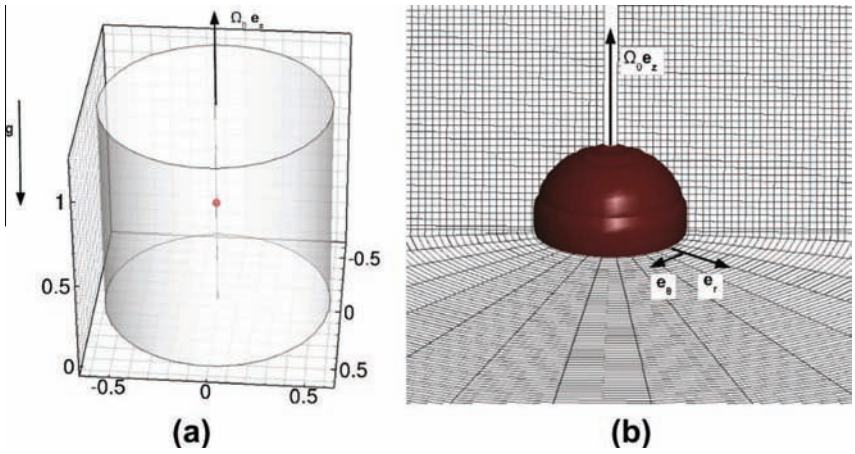

Fig. 10. Numerical setup with (a) a global view of the sphere within the cylindrical computational domain, and (b) a close-up view of the grid used in the vicinity of the sphere here materialized by iso-value of the solid volume fraction $\alpha = 0.1$.

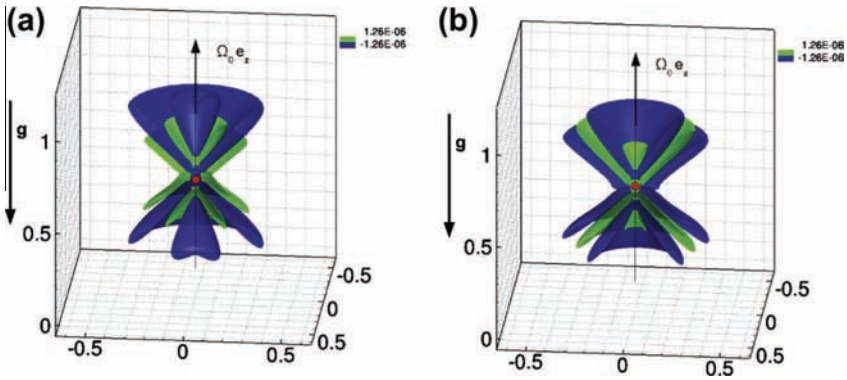

Fig. 11. Iso-surfaces of density fluctuations $\delta\rho$ generated by an oscillating sphere in a rotating stratified fluid at (a) $t\sigma/(2\pi) = 4.7$ and (b) $t\sigma/(2\pi) = 5.2$ for $Re = 100, Fr = 0.8, \mathcal{C} = 0.316$ and $A_0/R = 1$. Iso-surfaces $\delta\rho = \pm 1.26 \times 10^{-6}$ are plotted on half the computational domain in order to show the sphere location. Here, the simulation is three-dimensional.

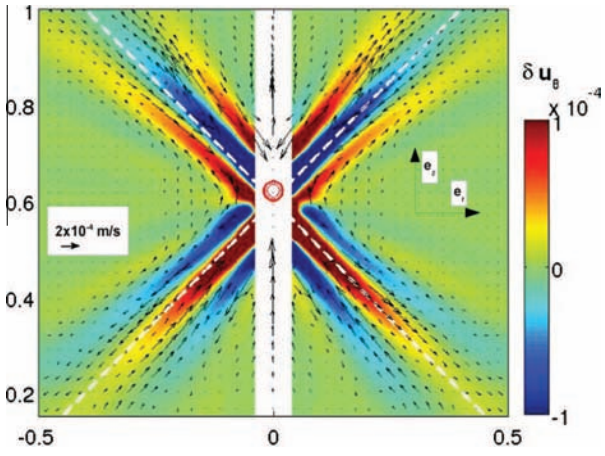

Fig. 12. Azimuthal component of the velocity fluctuation field $\delta\mathbf{u}$ (same parameters as Fig. 11(b)). The vectors represent the corresponding (r, z)-components of $\delta\mathbf{u}$. The location of the sphere is materialized by selected iso-values of α. The white dashed lines correspond to the direction of propagation obtained from (39). Note that the near flow field of the sphere and color background around the z-axis are not shown for clarity.

of the above mentioned authors, a constant velocity of the sphere is imposed and the drag force is measured. Some of their results are reproduced in Fig. 17 for $Re = 200, 0.2 < Fr < 200$, and $Sc = 700$. For $Fr = 0.8$ (i.e. $1/Fr = 1.25$), the expected drag coefficient lies in the range $C_D \approx 3 - 4$, approximately. This is of the same order of magnitude as the value of the maximum drag coefficient found in the present simulation (Fig. 13). It must be stressed that the present comparison is only qualitative since we simulate the flow of an oscillating sphere, while Hanazaki et al. [30] compute the flow around a translating particle. In addition, we set the object and the fluid to be initially in solid body-rotation while in the simulation of these authors, the fluid is initially at rest.

Contours of the azimuthal component of vorticity in the vicinity of the sphere are plotted in Fig. 14 over half an oscillation cycle. Two regions can be identified, namely a far-field region in which the waves of Saint-Andrew cross-shape are visible via the sharp transition of the vorticity sign, and a near-field region in which vorticity is generated at the sphere surface. The near-field region is observed to extend up to a distance of one diameter away from the sphere centroid, approximately, in agreement with experimental observation (Fig. 14(f); [64]). Note that the structure of the wake is different from the constant-density non-rotating lower Re-case (see e.g. Fig. 6) indicating a non-negligible influence of stratification/rotation not only on the far field but also on the local flow structure around the moving object.

3.2.2. Flow past a sphere dragged vertically in a stratified fluid

Experiments of such flows (see e.g. [46,60]) have shown that the axisymmetric flow is retained for Reynolds numbers well above 200, which is the upper limit for axisymmetry in homogeneous flow, because vortex shedding and transition to turbulence can

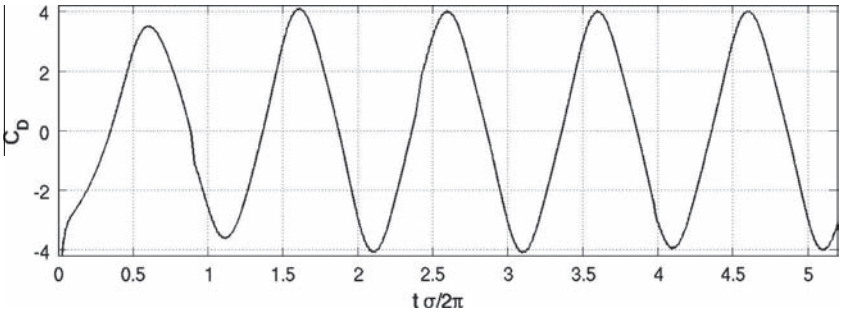

Fig. 13. Time evolution of the drag coefficient C_D on a oscillating sphere in a rotating stratified fluid ($Re = 100, Fr = 0.8, \mathcal{C} = 0.316, A_0/R = 1$).

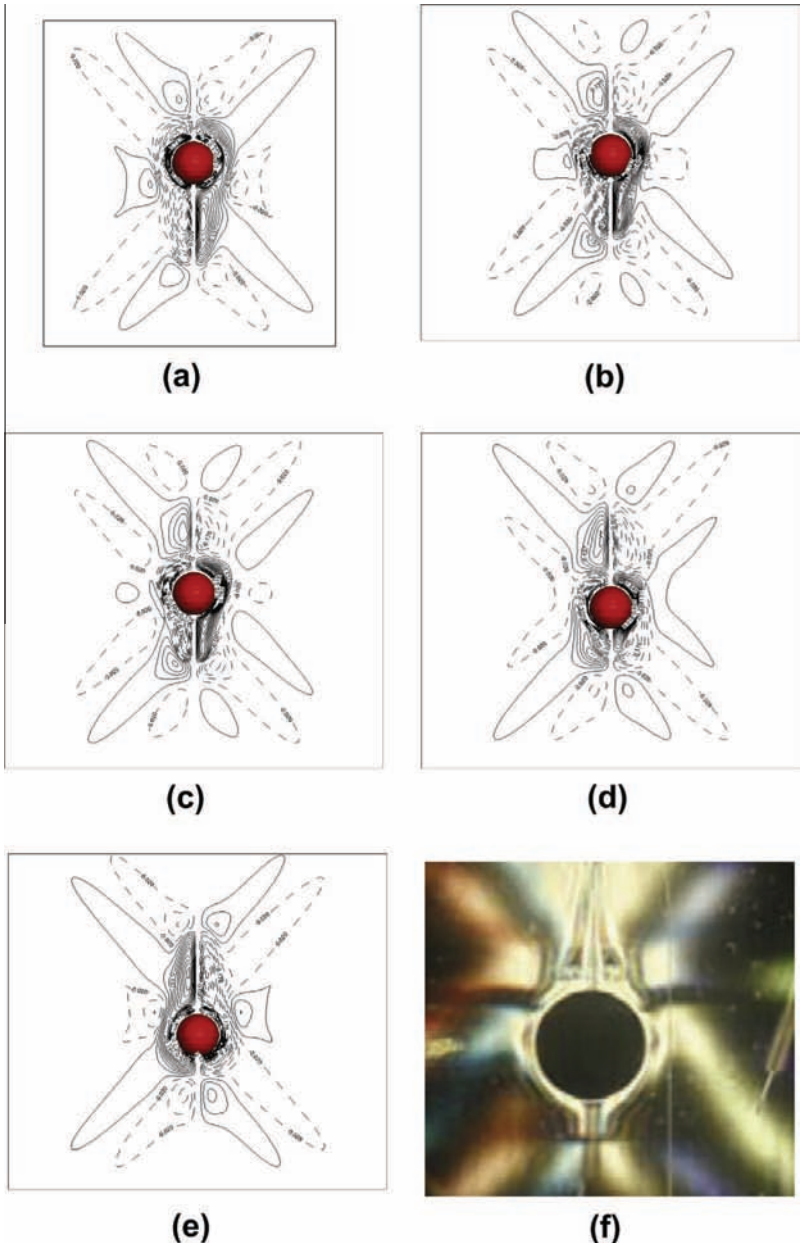

Fig. 14. Contours of the azimuthal component of vorticity over half an oscillation cycle in the vicinity of the sphere obtained from the three-dimensional simulation. The time instances of the snapshots are such that $\sigma t = \phi[2\pi]$ with $(a)\ \phi = 0$; $(b)\ \phi = 4\pi/13$; $(c)\ \phi = 6\pi/13$; $(d)\ \phi = 9\pi/13$; $(e)\ \phi = \pi$. The sphere is materialized by the iso-surface of the solid volume fraction $\alpha = 0.1$. (e) Experimental visualization of Chashechkin [12] for $Re \approx 300, Fr \approx 0.5, \mathcal{C} = 0$ and $A_0/R = 1.2$.

be inhibited by stratification. Axisymmetric standing vortex usually found in homogeneous fluids at moderate Reynolds numbers ($25 \leqslant Re \leqslant 200$) is completely collapsed by stable stratification, generating a strong vertical jet. Recently, Torres et al. [60] and Hanazaki et al. [30] performed numerical simulations thanks to a boundary-fitted approach using Boussinesq approximation. They showed that for $Re = 200$, the complete collapse of the vortex occurs at Froude number $Fr \leq 19$, and the critical Froude number decreases slowly as Re increases. The Froude number and the Reynolds number are here defined by $Fr = 2U_0/ND$ and $Re = \rho U_0 D/\mu$ with U_0 being the descent velocity of the sphere, N the Brunt-Väisälä frequency, D the sphere diameter and μ the dynamic viscosity of the fluid.

Two configurations are investigated here, namely $(Re, Fr) = (200, 2)$ and (200,20). The simulations are performed on the same two-dimensional axisymmetric domain as in Section 3.1.4 with twice the resolution (the $20D \times 40D$ (r, z)-domain is discretized with 256×1600 grid points) so that there are 40 cells per sphere diameter. Free-slip and Neumann boundary conditions are imposed at all boundaries for the velocity and density, respectively. The sphere is initially located at a distance $7R$ from the upper wall and the fluid is initially at rest. A $t > 0$, the sphere is dragged at an imposed constant velocity U_0 in the direction opposite to the density gradient. It should be noted that contrary to the simulations of Torres et al. [60] and Hanazaki et al. [30], the present simulation does not make use of Boussinesq approximation.

We plot in Fig. 15 isopycnals and streamlines in the vicinity of the sphere for the case $(Re, Fr) = (200, 20)$, when the sphere has crossed a distance of $13D$. The figure shows that at this relatively weak stratification, a standing vortex exists just as in homogeneous fluids. This is in line with experimental observations and the results of Hanazaki et al. [30] for which qualitative agreement is found (see Fig. 15c). Note that small steps in the density iso-contours can be observed in the region of sharp gradients, separating the wake of the sphere from the far-field (Fig. 15a). These patterns are a consequence of the Flux-Corrected-Transport scheme used for solving the transport equation of density. This family of shock-capturing scheme contains an anti-diffusive step which sharpen the density distribution when the typical thickness of the density gradient is of the grid size. Increasing stratification causes complete vortex collapse of the wake and the generation of a long narrow filament or jet. This is illustrated in Fig. 16 when $(Re, Fr) = (200, 2)$. The density and flow structure is well reproduced by the present immersed-boundary method. Note that some cusps can be observed in Fig. 16a at a distance of 3-6D downstream the rear part of the sphere, in the vicinity of the thin axisymmetric jet generated in the wake. Similar cusps were observed by Hanazaki et al. [30] for similar physical parameters but a much finer resolution that the present one (see their Fig. 9a).

We plot in Fig. 17 the time evolution of the drag coefficient. In order to compare our results with those of Torres et al. [61] and Hanazaki et al. [30] who solved the equations for the perturbed density and pressure fields, we remove the contribution of the unperturbed hydrostatic pressure. To be explicit, the instantaneous drag coefficient C_D is here calculated as,

$$C_D = \frac{\widehat{F}_D}{\frac{1}{2}\rho_0 U_0^2 \pi R^2}, \tag{41}$$

$$\widehat{F}_D = F_D - \vartheta_p \frac{\partial \rho_e}{\partial z} g(z_0 - z_p), \tag{42}$$

with $F_D = -\int_{\vartheta_p} \rho \mathbf{f} d\vartheta$ being computed the same way as (30) and z_p the local vertical position of the sphere (the detailed derivation of (42) is given in appendix). We find a very good agreement with the results reported by Torres et al. [61] and Hanazaki et al. [30] in the case of zero-to-low stratification ($Fr = 20$) and reasonable agreement in the case of moderate-to-large stratification ($Fr = 2$). In the latter case, the discrepancy may be due to the fact that in the present case, the fluid is non-diffusive ($Sc \gg 1$) contrary to the results of these authors for which $Sc = 700$. In particular, Torres et al. [60] mention that in the case of non-diffusive fluids, the density contours accumulate ahead of the particle (see e.g. Fig. 16(a)) and prevent the steady state condition to be reached, as observed in Fig. 17. We note in passing that the drag coefficient in the $Fr = 2$-case is slightly but noticeably increasing with time for both the present approach and the boundary-fitted method of Torres

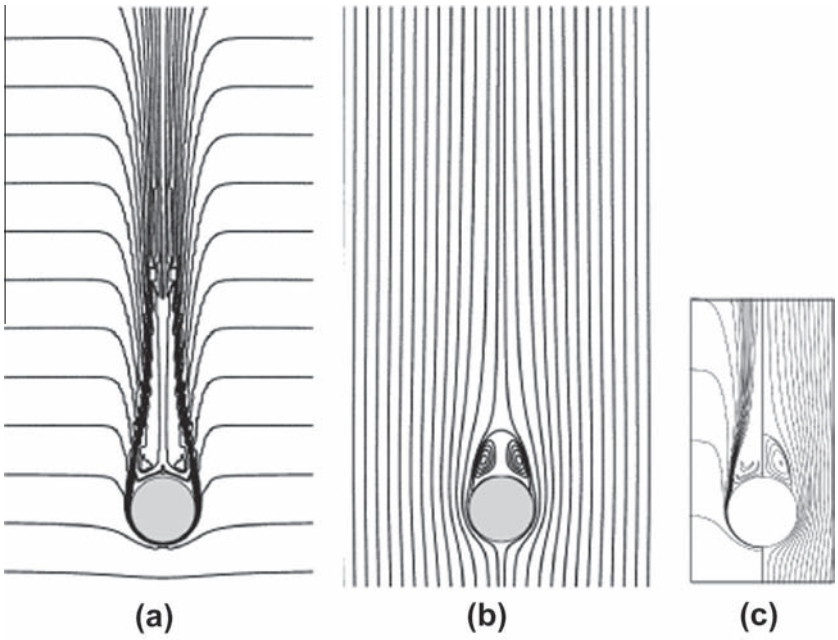

Fig. 15. Isopycnals (a) and streamlines (b) when $Fr = 20, Re = 200$, and $Sc \gg 1$ at $tU_0/R = 52$ (the sphere has crossed a distance of $13D$). For comparison, results of Hanazaki et al. [30], obtained for $Fr = 20, Re = 200$, and $Sc = 700$ with a boundary-fitted approach are plotted in (c). Here, the simulation is two-dimensional axisymmetric.

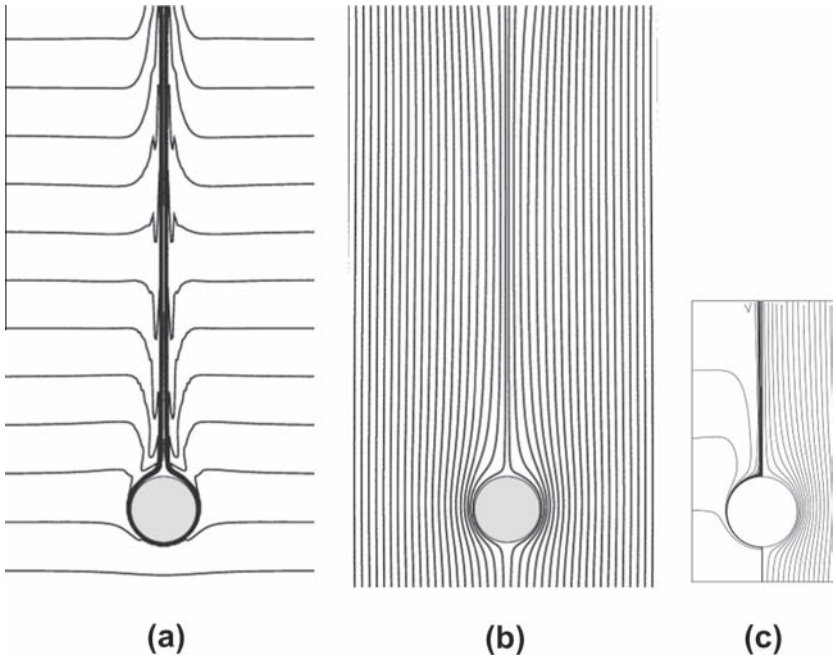

Fig. 16. Same as Fig. 15 for $Fr = 2$ and $Re = 200$.

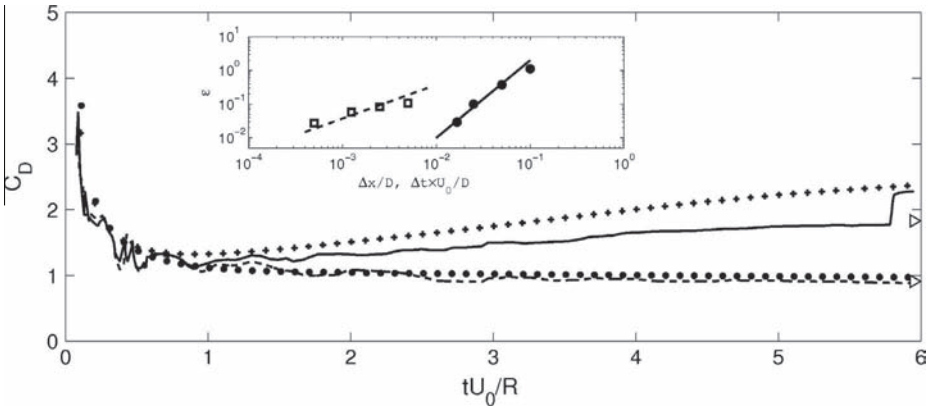

Fig. 17. Time evolution of the total drag coefficient C_D. Present method ($Re = 200$, $Sc \gg 1$): +, $Fr = 2$; •, $Fr = 20$. Simulations from the boundary-fitted method of Torres et al. [61] ($Re = 200, Sc = 700$): _____, $Fr = 2$; - - - -, $Fr = \infty$. The upper and lower triangles indicate the value of C_D reported in Fig. 13 of Hanazaki et al. [30] for $Fr = 2$ and $Fr = 20$, respectively. Inset: Error computed from the value of C_D at time $tU_0/R = 5$ as a function of (•) spatial resolution and (□) time step. The reference value of C_D used for the spatial and temporal convergence analysis is the one obtained with ($\Delta r/D = 1.25 \times 10^{-3}; \Delta t \times U_0/D = 2.5 \times 10^{-2}$) and ($\Delta r/D = 2.5 \times 10^{-2}; \Delta t \times U_0/D = 2.5 \times 10^{-4}$), respectively. The dashed and solid lines indicate first- and second-order convergence, respectively.

et al. [61], at least up to $tU_0/R < 5$. From this time, the drag coefficient reported by these authors seems to reach a plateau contrary to our results, however, this plateau is mitigated by an abrupt jump a time $tU_0/R \approx 6$.

We also plot in Fig. 17 the error computed from the value of C_D at time $tU_0/R = 5$ as a function of the spatial resolution and the time step, and find a first- and second-order convergence, respectively, similar to that found in the convergence study performed in the homogeneous case (see Fig. 7(b)). Note that the observed effective temporal and spatial order-of-accuracy of the present method with the IBM treatment and a fluid of variable density is observed to be somewhat lower than the expected second order-of-accuracy of the Crank–Nicolson/Runge–Kutta scheme. Firstly, this may be attributed to the use of the FCT scheme for the transport equation of the density. In the case of variable density flow with surface tension effects and no IBM treatment, Bonometti and Magnaudet [6] found a spatial order-of-accuracy of 1–1.5 approximately, when using the FCT scheme. Second, recall that the present IBM treatment does not make use of markers as in Uhlmann [63] or interpolation operators for the pressure and boundary force as in Taira and Colonius [58] and is likely to lower the effective order-of-accuracy. This latter point was recently confirmed by Guy and Hartenstine [27] who demonstrated that direct forcing IBM were generally first-order accurate, the order of accuracy being able to increase up to second-order depending on the local 'smoothness' of the solution across the immersed boundary.

The distribution of the vertical velocity near the sphere's equator is given in Fig. 18(a) for various spatial resolutions and in Fig. 18(b) for two values of the Froude number, namely $Fr = 2$ and $Fr = 20$. We observe that the momentum boundary layer is roughly independent of the spatial resolution for $D/\Delta r = 40$. At lower spatial resolution the region of influence of the immersed object is increased as the thickness of the transition region of the solid volume fraction α is increased. As a consequence, the location of the maximum velocity is artificially shifted away from the particle surface. In Fig. 18(b), the present results for $D/\Delta r = 40$ are

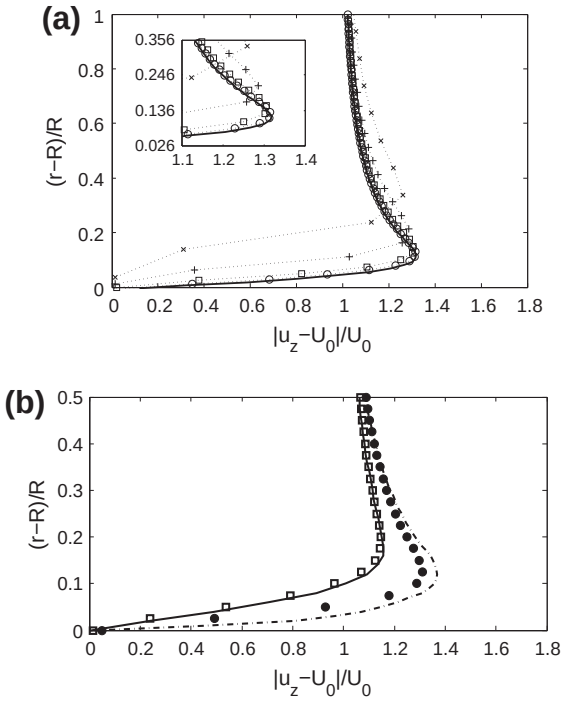

Fig. 18. Distribution of the vertical velocity near the sphere's equator. (a) Results obtained with the present method and various spatial resolutions: $\times, D/\Delta r = 10$; $+, D/\Delta r = 20$; $\square, D/\Delta r = 40$; $\circ, D/\Delta r = 60$; _____, $D/\Delta r = 80$. Here, $Re = 200, Sc \gg 1, Fr = 2$ and $tU_0/R = 5$. Inset: close-up view near the velocity maximum. (b) Present method ($Re = 200, Sc \gg 1, tU_0/R = 52, D/\Delta r = 40$): $\square, Fr = 20$; $\bullet, Fr = 2$. Simulations from the boundary-fitted method of Torres et al. [60] for which $Re = 200$, $Sc = 700$: _____, $Fr = 20$; - · - · -, $Fr = 2$.

compared to those obtained from the boundary-fitted approach of Torres et al. [60] who used a much finer grid in the sphere region. Very good agreement is found for $Fr = 20$ and a reasonable agreement is observed for $Fr = 2$, the difference of the maximum velocity being less than 5%.

3.2.3. Sphere sedimenting in a stratified fluid at $Re = \mathcal{O}(10^3)$

Here, the sedimentation of a sphere in a linearly stratified viscous fluid, as defined in (34), is considered for two different density ratios, namely $\rho_p/\rho_0 = 4.6$ and 6.1, ρ_0 being a reference density defined by the fluid density at the initial vertical location z_0 of the particle centroid and ρ_p being the density of the particle. We set the physical properties of the particle and the fluid so the Archimedes number is $Ar = 2.3 \times 10^5$ and 3.3×10^5, respectively, and the Froude number $Fr = 4.3$. For comparison, we also computed the constant-density case. The simulation is performed in a three-dimensional domain of $6.3R \times 6.3R \times 51.5R$ size with $64 \times 64 \times 512$ grid points. The spatial resolution is uniform in all directions corresponding to 20 grid points per particle diameter. No-slip (resp. Neumann) boundary conditions are imposed at the top and bottom walls for the velocity (resp. density) while periodic conditions are set for the lateral walls. Note that other boundary conditions could have been used, namely free-slip conditions for the velocity, without changing the results significantly. In the present case, using periodic boundary conditions along the side walls corresponds to simulating the sedimentation of a regular horizontal array of spherical particles in a stratified fluid. The sphere centroid is initially located at a distance of $2.2R$ from the upper wall and the fluid is initially at rest.

Note that here the size of the computational domain is rather small. As a consequence, confinement effects may modify the sedimentation velocity of the sphere, and additionally the perturbation of the density field due to the motion of the sphere may generate internal waves, the propagation of which being influenced by the side walls. In addition, recall that the spatial resolution is such that there are 20 grid points per particle diameter. The convergence study of Section 3.2.2 suggests that this spatial resolution may be somewhat low to fully capture the flow near the sphere surface. Here, however, we are interested in showing the capability of the present approach to simulate the three-dimensional flow around a freely-moving object in a stratified fluid, so a moderate size of the computational domain and spatial resolution were chosen.

Fig. 19 shows the time evolution of the vertical distance crossed by the sedimenting sphere and the corresponding local particle Reynolds number in the three configurations considered here (constant-density flow with $\rho_p/\rho_0 = 4.6$, stratified flow with $\rho_p/\rho_0 = 4.6$ and 6.1). For all cases, the particle quickly accelerates at early times to reach a particle Reynolds number of about 1300-1800 ($t \leq 7$). Contrary to the constant-density case, the speed of the particle in the stratified fluid abruptly drops down due to the enhanced drag stemming from the buoyancy of a tail of light fluid dragged down by the sphere and the vanishing buoyancy force which decreases as the particle gets closer to the vertical neutral buoyancy level z_n corresponding to $\rho = \rho_p$. It is worth noting that in the case $\rho_p/\rho_0 = 4.6$ and $Fr = 4.3$ the particle speed alternatively changes sign, leading to slight but noticeable lift-up of the particle centroid (see Fig. 19 at times $t = 25$, 33, 55 and 70). The time at which the particle speed decreases is larger for the particle of larger density ratio since inertia and buoyancy forces are larger in this case. As expected, the particle eventually approaches to the level z_n, however, the duration of approach is relatively large since both the drag force and buoyancy forces are slowly decreasing due to a slow decrease in local velocity and density contrast, respectively.

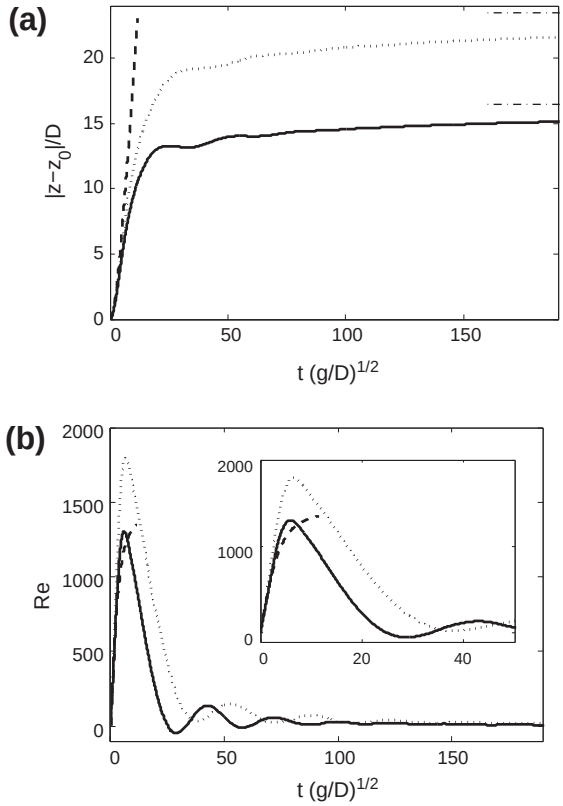

Fig. 19. Time evolution of (a) the vertical distance crossed by the sedimenting sphere and (b) local particle Reynolds number: (- - - -), $Fr = \infty, \rho_p/\rho = 4.6$; (_____), $Fr = 4.3$, $\rho_p/\rho = 4.6$; (· · · · · ·), $Fr = 4.3$, $\rho_p/\rho = 6.1$. The dash-dotted lines indicate the location of the neutral buoyancy level for which $\rho = \rho_p$. Here, the simulation is three-dimensional.

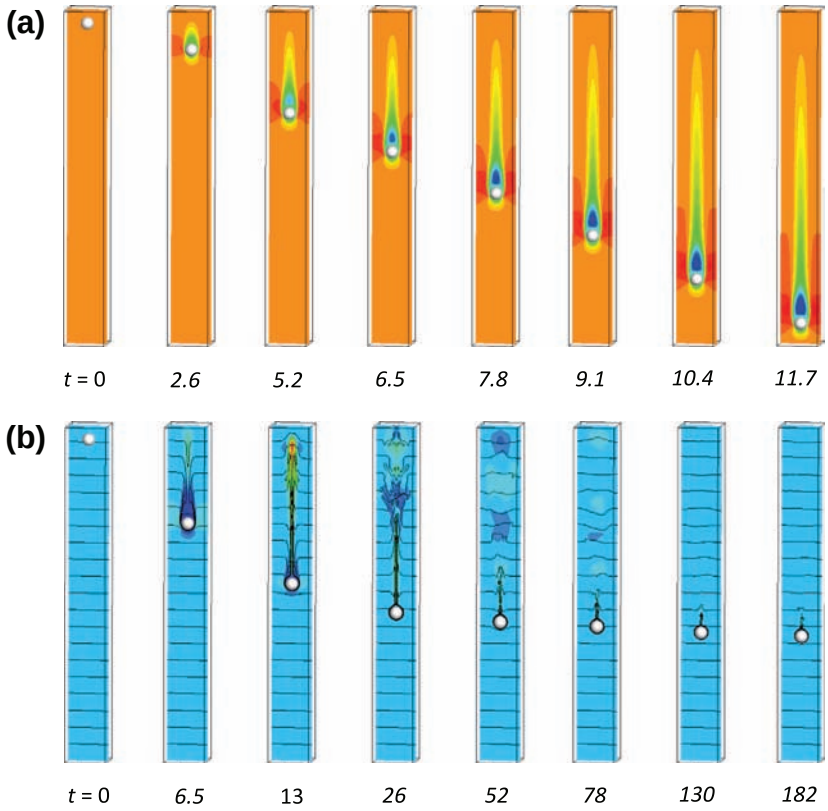

Fig. 20. Three-dimensional simulation of the sedimentation of a sphere at $Re = \mathcal{O}(10^3)$ in (a) a constant-density flow ($Fr = \infty$) and (b) a linearly stratified flow ($Fr = 4.6$). In both cases, $Ar = 2.3 \times 10^5$ and $\rho_p/\rho = 4.6$. Instantaneous distribution of the vertical velocity field in the range (a) [−3.9 0.5] and (b) [−0.5 2.3], respectively. Isopycnals are also plotted in frame (b). Here time is scaled by $\sqrt{D/g}$ and velocity is scaled by $\sqrt{gD}$.

The local flow structure is shown in Fig. 20 for both the constant-density case and the stratified ambient case at $\rho_p/\rho_0 = 4.6$. A long wake is generated in the $Fr = \infty$ (constant-density) case with a recirculation zone of about $2D$ downstream the sphere. In contrast, the wake behind the sphere which sediments in the stratified ambient develops only at early times ($t \leqslant 7$) and quickly collapses. At early times, the structure of the wake is roughly similar to that reported in Fig. 6c of Bayareh et al. [5] who computed the motion of a particle at a somewhat larger Froude number, namely $Fr = 11.2$. As the wake collapses, a thin upward jet is created and isopycnals are lifted-up ($t = 13$), generating internal waves and local mixing, in agreement with observations [60]. As the particle slowly goes towards the level z_n, internal waves are damped by viscous dissipation.

4. Summary and conclusions

A simple immersed-boundary method has been used for simulating constant- and stratified-density flows past complex moving boundaries. The method is based on a direct forcing approach in which the solid objects are represented by a continuous solid volume fraction. Two- and three-dimensional canonical flows are simulated and the results are compared with available analytical, experimental or numerical data in order to show the accuracy of the current approach. In the configurations considered here, the present method is capable of accurately describing the flow in the region close to the immersed boundary even though it does not make use of any high-order interpolation technique or Lagrangian marking of the boundary. Simulations are performed for stratified flows with moving boundaries. The current approach, which makes use of a shock-capturing scheme for the transport of density, is observed to describe reasonably well the temporal variation of the hydrodynamic forces as well as the sharp spatial gradients of density, despite the somewhat moderate spatial resolution used in the vicinity of the immersed boundary. Here, we only considered a single object in order to establish the relevancy of the present approach in academic configurations. It is however possible to extend the present approach to multiple non-spherical objects, provided a suitable collision model is implemented. This is beyond the scope of the present paper, and is left for future work.

Acknowledgments

BB would like to acknowledge support from the STAE Fundation ITAAC project. We thank Franck Auguste for having provided the results concerning the fall of the sphere obtained via the boundary-fitted version of the JADIM code in Section 3.1.4. TB and LL thank Annaig Pedrono, Dominique Legendre, Vincent Laval and Melody Vlieghe for their support in the development of the immersed-boundary version of the Navier–Stokes solver used in this research. TB thanks Markus Uhlmann and Jacques Magnaudet for fruitful discussions. Some of the computational time was provided by the Scientific Groupment CALMIP (Projects P1027, P1124), the contributions of which is greatly appreciated.

Appendix A

In this appendix, we give details about the derivation of the drag force (42) used in Section 3.2.2. Here, we assume that the sphere is dragged at a constant velocity. The drag force acting on a body of surface S_p and volume ϑ_p is $\int_{S_p} \tau \cdot \mathbf{n} dS$ with $\tau = -P\mathbf{I} + \mu(\nabla\mathbf{V} + \nabla\mathbf{V}^T)$ being the hydrodynamic stress tensor and $\mathbf{n}$ the outward pointing vector normal to the sphere surface. Integrating momentum and kinematic momentum laws (1) and

(2) for the fluid on ϑ_p and using the fact that the sphere velocity is here constant, one can write (see e.g. Eqs. (16)–(18))

$$\int_{S_p} \tau \cdot \mathbf{n} dS = -\int_{\vartheta_p} \rho \mathbf{f} d\vartheta - \bar{\rho}\vartheta_p \mathbf{g}. \tag{43}$$

Decomposing the pressure field P into two parts, namely an unperturbed hydrostatic pressure p_e and a perturbation, and using the Boussinesq approximation one can express the total drag force as

$$\int_{S_p} \tau \cdot \mathbf{n} dS = -\int_{S_p} p_e \mathbf{n} dS + \int_{S_p} \hat{\tau} \cdot \mathbf{n} dS, \tag{44}$$

where $\hat{\tau}$ include the perturbation pressure and the viscous stress tensor. Note that $\widehat{F}_D = \int_{S_p} \hat{\tau} \cdot \mathbf{n} dS$ is the drag force computed in Torres et al. [60,61] and Hanazaki et al. [30]. Using the fact that the hydrostatic pressure p_e reads (see Eqs. (16)–(18))

$$p_e(z) = -\rho_0 g z + \frac{1}{2}\frac{\partial \rho_e}{\partial z} g z(z - 2z_0), \tag{45}$$

one can calculate the first term in the right hand side of (44)

$$-\int_{S_p} p_e \mathbf{n} dS = \vartheta_p \frac{\partial \rho_e}{\partial z} g(z_0 - z_p) - \rho_0 \vartheta_p g, \tag{46}$$

with z_p being the local vertical position of the sphere. Eliminating τ in (43) and (44), and using (46), one finds

$$\begin{aligned} \widehat{F}_D &= \int_{S_p} \hat{\tau} \cdot \mathbf{n} dS \\ &= -\int_{\vartheta_p} \rho \mathbf{f} d\vartheta - \vartheta_p \frac{\partial \rho_e}{\partial z} g(z_0 - z_p) - (\bar{\rho} - \rho_0)\vartheta_p g. \end{aligned} \tag{47}$$

Finally, the averaged fluid density in the region of the particle $\bar{\rho}$ at an arbitrary time is in fact that initially located inside the particle at time $t = 0$ (for $z_p = z_0$). This patch of density has been transported 'inside' the dragged particle (see Eq. (3)). Computing the initial average fluid density $\bar{\rho}(t = 0)$ in the region ϑ_p of the particle, one finds $\bar{\rho} = \rho_0$ leading to

$$\widehat{F}_D = -\int_{\vartheta_p} \rho \mathbf{f} d\vartheta - \vartheta_p \frac{\partial \rho_e}{\partial z} g(z_0 - z_p). \tag{48}$$

References

[1] Apte S, Martin M, Neelesh A, Patankar N. A numerical method for fully resolved simulation (frs) of rigid particleflow interaction in complex flows. J Comput Phys 2009;228:2712–38.
[2] Ardekani A, Dabiri S, Rangel R. Collision of multi-particle and general shape objects in a viscous fluid. J Comput Phys 2008;227:10094–107.
[3] Auguste F. Instabilites de sillage generees derriere un corps solide, fixe ou mobile dans un fluide visqueux. Ph.D. thesis, University of Toulouse; 2010.
[4] Balay S, Brown J, Buschelman K, Gropp WD, Kaushik D, Knepley MG, et al. PETSc Web page; 2013. <Http://www.mcs.anl.gov/petsc>.
[5] Bayareh M, Doostmohammadi A, Dabiri S, Ardekani AM. On the rising motion of a drop in stratified fluids. Phys Fluids 2013;25:103302.
[6] Bonometti T, Magnaudet J. An interface-capturing method for incompressible two-phase flows: validation and application to bubble dynamics. Int J Multiphas Flow 2007;33:109–33.
[7] Boris JP, Book DL. Flux-corrected transport: I. SHASTA, a fluid transport algorithm that works. J Comput Phys 1973;18:248–83.
[8] Brown DL, Cortez R, Minion ML. Accurate projection methods for the incompressible Navier–Stokes equations. J Comput Phys 2001;168:464–99.
[9] Calmet I. Analyse par simulation des grandes echelles des mouvements turbulents et du transfert de masse sous une interface plane. Ph.D. thesis, Inst. Nat. Polytech., Toulouse; 1995.
[10] Calmet I, Magnaudet J. Large-eddy simulation of high-schmidt number mass transfer in a turbulent channel flow. Phys Fluids 1997;9:438–55.
[11] Chang E, Maxey MR. Unsteady flows about a sphere at low to moderate reynolds number. Part 1: Oscillatory motion. J Fluid Mech 1994;277:347–79.
[12] Chashechkin Y. The complex structure of wave fields in fluids. Proc IUTAM 2013;8:65–74.
[13] Chen CY, Meiburg E. Miscible displacements in capillary tubes: influence of Korteweg stresses and divergence effects. Phys Fluids 2002;14:2052–8.
[14] Clift R, Grace JR, Weber ME. In: Bubbles drops and particules. Academic Press; 1978.
[15] Cook AW, Dimotakis PE. Transition stages of Rayleigh–Taylor instability between miscible fluids. J Fluid Mech 2001;443:69–99.
[16] Coutanceau M, Bouard R. Experimental determination of the main features of the viscous flow in the wake of a circular cylinder in uniform translation. Part 1: Steady flow. J Fluid Mech 1977;79:231–56.
[17] Cushman-Roisin B. Lower and upper bounds on internal-wave frequencies in stratified rotating fluid. Phys Rev Lett 1996;77:4903–5.
[18] Dennis S, Chang G. Numerical solutions for steady flow past a circular cylinder at reynolds number up to 100. J Fluid Mech 1970;42:471–89.
[19] Doostmohammadi A, Ardekani AM. Interaction between a pair of particles settling in a stratified fluid. Phys Rev E 2013;88:023029.
[20] Fadlun E, Verzicco R, Orlandi P, Mohd-Yusof J. Combined immersed-boundary finite-difference methods for three-dimensional complex flow simulations. J Comput Phys 2000;161:35–60.
[21] Fedkiw R, Aslam T, Merriman B, Osher S. A non-oscillatory eulerian approach to interfaces in multimaterial flows (the ghost fluid method). J Comput Phys 1999;152:457–92.
[22] Flynn M, Onu K, Sutherland B. Internal wave excitation by vertically oscillating sphere. J Fluid Mech 2003;494:65–93.
[23] Glowinski R, Pan T, Hesla T, Joseph D. A distributed lagrange multiplier/fictitious domain method for particulate flows. Int J Multiphase Flow 1999;25:755–94.
[24] Greenspan H. The theory of rotating fluids. Cambridge University Press; 1969.
[25] Guermond JL, Minev P, Shen J. An overview of projection methods for incompressible flows. Comput Methods Appl Mech Eng 2006;195:6011–45.
[26] Guermond JL, Salgado A. A splitting method for incompressible flows with variable density based on a pressure Poisson equation. J Comput Phys 2009;228:2834–46.
[27] Guy RD, Hartenstine DA. On the accuracy of direct forcing immersed boundary methods with projection methods. J Comput Phys 2010;229:2479–96.
[28] Jones LE, Sandberg RD, Sandham ND. Direct numerical simulation of forced and unforced separation bubbles on an airfoil at incidence. J Fluid Mech 2008;603:175–207.
[29] Joseph D, Renardy Y. In: Fundamentals of two-fluid dynamics, Part II. New York: Springer; 1992.
[30] Hanazaki H, Konishi K, Okamura T. Schmidt-number effects on the flow past a sphere moving vertically in a stratified diffusive fluid. Phys Fluids 2009;21:026602.
[31] Harlow F, Welch J. Numerical calculation of time-dependent viscous incompressible flow of fluid with free surface. Phys Fluids 1965;8:2182–9.
[32] Hendershott M. Impulsively started oscillations in a rotating stratified fluid. J Fluid Mech 1969;36:513–27.
[33] Hoarau Y, Braza M, Ventikos Y, Faghani D, Tzabiras G. Organized modes and the three-dimensional transition to turbulence in teh incompressible flow aroung a naca0012 wing. J Fluid Mech 2003;496:63–72.
[34] Iaccarino G, Verzicco R. Immersed boundary technique for turbulent flow simulations. Appl Mech Rev 2003;56:331–47.
[35] Kang S, Iaccarino G, Ham F. Dns of buoyancy-dominated turbulent flows on a bluff body using the immersed boundary method. J Comput Phys 2009;228:3189–208.
[36] Khadra K, Angot P, Parneix S, Caltagirone J. Fictitious domain approach for numerical modelling of Navier–Stokes equations. Int J Numer Meth Fluids 2000;34:651–84.
[37] Kim J, Kim D, Choi H. An immersed-boundary finite-volume method for simulations of flow in complex geometries. J Comput Phys 2001;171:132–50.
[38] Ladd A, Verberg R. Lattice–Boltzmann simulations of particlefluid suspensions. J Stat Phys 2001;104:1191–251.
[39] Le H, Moin P. An improvement of fractional step methods for the incompressible Navier–Stokes equations. J Comput Phys 1991;92:369–79.
[40] Linnick M, Fasel H. A high-order immersed interface method for simulating unsteady incompressible flows on irregular domains. J Comput Phys 2005;204:157–92.
[41] Liseikin V. Grid generation methods. Berlin: Springer-Verlag; 1999.
[42] Magnaudet J, Rivero M, Fabre J. Accelerated flows past a rigid sphere or a spherical bubble. Part 1: Steady straining flow. J Fluid Mech 1995;284:97–135.
[43] Mittal R, Dong H, Bozkurttas M, Najjar F, Vargas A, Von Loebbecke A. A versatile sharp interface immersed boundary method for incompressible flows with complex boundaries. J Comput Phys 2008;227:4825–52.
[44] Mittal R, Iaccarino G. Immersed boundary methods. Ann Rev Fluid Mech 2005;37:239–61.
[45] Mougin G, Magnaudet J. Path instability of a rising bubble. Phys Rev Lett 2001;88:014502.
[46] Mowbray D, Rarity B. The internal wave pattern produced by a sphere moving vertically in a density stratified liquid. J Fluid Mech 1967;30:489–95.
[47] Nishioka M, Sato H. Measurements of velocity distributions in the wake of a circular cylinder at low reynolds numbers. J Fluid Mech 1974;65:97–112.
[48] Odar F, Hamilton W. Forces on a sphere accelerating in a viscous fluid. J Fluid Mech 1963;18:302–14.
[49] Park J, Kwon K, Choi H. Numerical solutions of flow past a circular cylinder at reynolds numbers up to 160. KSME Int J 1998;12:1200–5.
[50] Patankar N, Sharma N. A fast projection scheme for the direct numerical simulation of rigid particulate flows. Commun Numer Methods Eng 2005;21:419–32.

[51] Patankar N, Singh P, Joseph D, Glowinski R, Pan T. A new formulation of the distributed lagrange multiplier/fictitious domain method for particulate flows. Int J Multiphase Flow 2000;26:1509–24.
[52] Peacock T, Weidman P. The effect of rotation on conical wave beams in a stratified fluid. Exp Fluids 2005;39:32–7.
[53] Peskin C. Numerical analysis of blood flow in the heart. J Comput Phys 1977;25:220.
[54] Peskin C. The immersed boundary method. Acta Numer 2000;11:479–517.
[55] Rai M, Moin P. Direct simulations of turbulent flow using finite-difference schemes. J Comput Phys 1991;96:15–53.
[56] Sarthou A, Vincent S, Caltagirone J, Angot P. Eulerian–Lagrangian grid coupling and penalty methods for the simulation of multiphase flows interacting with complex objects. Int J Numer Methods Fluids 2008;56:1093–9.
[57] Sutherland B, Dalziel S, Hughes G, Linden P. Visualisation and measurement of internal waves by synthetic schlieren. Part 1: Vertically oscillating cylinder. J Fluid Mech 1999;399:93–126.
[58] Taira K, Colonius T. The immersed boundary method: a projection approach. J Comput Phys 2007;225:2118–37.
[59] Thompson J, Warsi ZU, Mastin C. Numerical grid generation, foundations and applications. New York: Elsevier; 1985.
[60] Torres C, Hanazaki H, Ochoa J, Castillo J, Van Woert M. Flow past a sphere moving vertically in a stratified diffusive fluid. J Fluid Mech 2000;417:211–36.
[61] Torres C, Ochoa J, Castillo J, Van Woert M. Initial flow field of stratified flow past an impulsively started sphere. Appl Numer Math 2000;40:235–44.
[62] Tritton D. Experiments on the flow past a circular cylinder at low reynolds numbers. J Fluid Mech 1959;6:547–67.
[63] Uhlmann M. An immersed boundary method with direct forcing for the simulation of particulate flows. J Comput Phys 2005;209:448–76.
[64] Voisin B, Ermanyuk E, Flor J. Internal wave generation by oscillation of a sphere, with application to internal tides. J Fluid Mech 2011;666:308–57.
[65] Yu Z, Shao X, Wachs A. A fictitious domain method for particulate flows with heat transfer. J Comput Phys 2006;217:424–52.
[66] Yuki Y, Takeuchi S, Kajishima T. Efficient immersed boundary method for strong interaction problem of arbitrary shape object with self-induced flow. J Fluid Sci Tech 2007;2:1–11.
[67] Zalesak S. Fully multidimensional flux-corrected transport algorithms for fluids. J Comput Phys 1979;31:335.